Ph.D Thesis

Isotopic analyses of water vapor and ammonia gas using cavity ring down spectroscopy for planetary exploration
惑星探査のための、キャビティリングダウン分光法を用いた水蒸気およびアンモニアガスの同位体分析

Junpei Murayama 村山純平
Department of Earth and Space Science,
Graduate School of Science, Osaka University

February, 2024

Abstract

In this thesis, we will demonstrate the effectiveness of the CRDS(cavity ring down spectroscopy) for isotopic measurement in planetary exploration. In Chapter 1 and 2, we introduce a significance of volatile element analysis on the planet environment including Moon's surface. Understanding of origin and dynamics of volatiles such as H_2O, CO_2 and NH_3 on the lunar surface is a crucial issue not only for the Lunar science but also for practical use of elements essential for long-term human life on the moon. For better understanding of the lunar volatiles, We have developed an on-site CRDS for analytical equipment on board the Moon Lander. CRDS is a useful tool for detecting trace levels of gaseous species due to its long optical path. As mentioned in Chapter , direct observation of lunar water and isotopic measurements using CRDS are expected in the LUPEX (Lunar Polar Exploration) mission, which is planned by JAXA (Japan Aerospace Exploration Agency) to launch in 2024 or later.

CRDS is characterized by its high sensitivity reaching the absorbance above 10^{-10}. The optical multiple reflections in CRDS allows for the detection of a trace amount of absorber less than 1 ng of water molecules in a 15 cm^3 cell, for example. More importantly for planetary use, significant miniaturization of CRDS can be achieved by using this feature, which permits a long effective optical path length that exceeds the cavity length, like several kilometers of optical path with a few centimeter cavity.

In Chapter 3, isotopes in water vapor are measured using a miniaturized CRDS with 5 cm cavity. We measured water standard samples with different D/H ratios, then applied Voigt profile fitting to the absorption spectra. Finally, a calibration line between the measured δD values and the literature values was obtained. The signal to noise ratio (SNR) of HDO peak at δD = -980 ‰ was 7.17, which was enough higher than the detection limit of 3σ. By using our miniaturized CRDS with high-sensitivity, we can identify H_2O molecules due to solar wind, in which D is depleted.

In Chapter 4, we developed a CRDS system with a cavity of 50cm for ammonia isotopic measurements. Ammonia is a significant industrial and agricultural resource, and it can be utilized as a transport medium for hydrogen fuel and as the fuel itself. Also, it is an important material in earth environment and outer plan-

ets. It has been studied spectroscopically for a long time, however, spectroscopic data on these isotopes is limited for a few wavelengths, and even when searching the HITRAN database, there is no comprehensive information. In this study, we performed experiments taking into account this point and measured the ratio of $^{15}N/^{14}N$ in gaseous ammonia. First of all, we searched the absorption lines experimentally, using $^{15}NH_3$ standard gas with the purity of 98 %. Three $^{15}NH_3$ absorption lines near 1.5 μm were chosen for this study. Wavelength was scanned by controlling the laser diode and we obtained absorption spectra for $^{15}NH_3$, then the spectra were compared with those of $^{14}NH_3$.

The measured spectra including absorption lines were evaluated using Allan variance to know the stability of measurement. One of the absorption lines was used to measure ^{15}N isotopic ratio in samples with different amounts of $^{15}NH_3$. Beforehand, we set the value of precision in nitrogen isotopic ratio at least $\delta^{15}N$ $\pm$ 100 ‰, considering the range of the isotopic ratio in the solar system. The calibration line we obtained from our measurements demonstrated a good agreement within the precision, which is up to 1 ‰ at 100 ‰ fractionation.

概要

本論文では、惑星探査での同位体測定における、CRDS(cavity ring down spectroscopy) と呼ばれる手法の有用性を、測定実験の結果とともに示す。1、2 章ではまず、月面を含む惑星環境において揮発性元素を測定分析することがいかに重要であるかを議論する。特に月面における H_2O、 CO_2、NH_3 といった揮発性分子の供給源や振る舞いを理解することは、人類にとっての長年のテーマであるだけにとどまらず、今後人類が月面に進出した際の足がかりとして非常に重要な情報となりうる。これら揮発性分子を測定・分析し、より深い理解を得るための装置として我々が推し進めているのが、CRDS という手法である。CRDS はその構造故に非常に長い光路長を持ち、微量なガス種を検出することに長けている。1 章で触れることになるが、JAXA(Japan Aerospace Exploration Agency) による探査計画である LUPEX(Lunar Polar Exploration) が 2024 以降にローンチされ、月面に存在する水を CRDS を用いて直接観測し、その同位体測定を行う予定である。

CRDS の特徴は、吸光度に置いて 10^{-10} に達する高い感度である。光の多重反射を用いる手法により、15 cm^3 のサンプルセルに含まれた、たった 1 ng の水分子も検出することができる。更に、限られたスペースの中で光路長を稼ぐことが可能なため、数 cm のキャビティで数 km の光路長といった、非常な小型化を実現できる。

3 章では、5cm のキャビティを採用した小型の CRDS を用いて、水蒸気の同位体測定を行った結果を示す。我々は異なる D/H 比をもつ標準資料を用意し、それらの吸収スペクトル測定を行い、そして Voigt 関数によるフィッティングを適用した。結果、既知の値との検量線を得たことに加え、δD = -980 ‰ の D が非常に枯渇したサンプルの同位体比を、検出限界を大幅に上回る SN 比 7.17 で測定することに成功した。月面に太陽から供給される水素原子は D に枯渇していると考えられており、月面微量水に対するそういった寄与を我々の CRDS で検出することが期待される。

4 章では、CRDS によるアンモニア同位体測定の結果を報告する。アンモニアは産業的にも非常に重要な資源であり、水素及び窒素の媒体としての役割も期待される分子である。もちろん地球環境においても重要な物質であり、その光学的性質についても長年研究がなされているものの、同位体という観点から見ると情報が限られている。本研究では、この観点から、CRDS を用いたアンモニア同位体測定の実現を目指した。まず最初に、98 % 純度の $^{15}NH_3$ ガスを用いて実際にスペクトル測定を行い、吸収線を探索した。その結果、1.5 μm 付近に、同位体測定に適した 3 つの $^{15}NH_3$ 吸収線候補を発見した。そのうちの 1 つを用い、測定したスペクトルから δ^{15}N を算出した上で、時系列測定においてアラン分散を求め、測定のばらつきを検証した。更に、異な

る $^{15}N/^{14}N$ 比となるような資料を用意し、検量線測定を行った。検量線は想定される精度として設定した 100‰ を下回るような良い一致を示し、100‰ 変動時における検量線のずれを約 ‰ に抑えられる結果となった。

Contents

1 Motivation : Moon water and LUPEX mission

For more than a century, the water's existence on the Moon's surface has been debated. In the 1960s, when the Apollo samples were studied, it was considered that the Moon's surface was completely dry. However, scientists have continued to seek signs of water.

Until today, a large number of observation were attempted. The Clementine Bistatic Radar Experiment yielded the first observations supporting the existence of the Moon water [1]. Lunar Prospector added further evidence by detecting neutron anomalies consistent with hydrogen deposits buried tens of centimeters under the regolith [2]. A water signal in the polar region was also discovered in the data from Cassini, which flew by the Moon in 1999 [3]. Deep Impact, of which purpose was comet Tempel 1 exploration, also flew by the Moon in 2009 and detected hydroxyl absorption signals strongest near the North Pole, consistent with < 0.5 wt% water [4]. In the same year, it was announced that Chandrayaan-1 had discovered a wide distribution of hydroxyl signals with Moon Mineralogy Mapper (M^3) [5], and the Lunar Crater Observation and Sensing Satellite (LCROSS) mission detected 5.6 ± 2.9 wt% water in the regolith covering Cabeus Crater, located in the south polar region [6].

Recently, the surficial hydroxyl signals from M^3 data were more discussed by Pieters et al. [5]. In 2014, researchers studying the Lunar Reconnaissance Orbiter (LRO)'s findings suggested that 3 to 14 wt% water ice could account for the anomalous reflectance observed in the permanent shadow of Shackleton Crater [7]. The data from Lunar Atmosphere and Dust Environment Explorer (LADEE) supported the existence of hydroxyl signals and implied an escape of water from the moon surface [9]. Further, the Chinese probe Chang'e-4 went to the far side of the Moon in 2020, and Chang'e-5 achieved in-situ observations using a lander and collected a return samples [10][11][12].

However, most observations of lunar water were from circum or near Moon orbit, but not on the ground. In addition, enough data to identify the isotopic composition has not yet been obtained. As mentioned later, isotopic measurement is necessary to identify the origin of the water. For the purpose, considering contamination by earth samples, we should have an on-site device with high-sensitive, simultaneously robust and light-weight. We propose that a spectroscopic

system is a good choice as a measurement method fulfilling the needs mentioned above.

The Lunar Polar Exploration (LUPEX) mission has been prepared by JAXA (Japan Aerospace Exploration Agency) and will be launched in 2024 or later. The main purpose of LUPEX is to search for water resources in the region of the lunar south pole. The moisture area on the moon is searched using a ground-penetrating radar mounted on a rover that travels on the lunar surface, as well as infrared vision and neutron spectroscopy. Next, the regolith at that location is excavated to obtain water-containing samples, which are then heated and the vapor is supposed to be studied by the CRDS and a time of flight mass spectrometer. The CRDS planned for LUPEX is based on the model used in this thesis. A miniaturized CRDS, which is described in the following Chapter 3, was designed during the Space Innovation Hub study organized by JAXA through 2016-2019, with Sinei Corporation, National Institute of Advanced Industrial Science and Technology, Osaka University, Ibaraki University, and Kagoshima University. Actually, this CRDS was designed as a trace moisture meter at atmospheric pressure at first. Then water content at low pressure and isotopic measurements were examined in this thesis considering the applications and use of this CRDS in the LUPEX mission.

2 Introduction

2.1 Isotopic fractionation

At first, I would like to introduce useful tools for the isotopic analysis. There are stable isotopes of Hydrogen (^{1}H(H) and ^{2}H(D)), Oxygen (^{16}O, ^{17}O and ^{18}O) and Nitrogen (^{14}N and ^{15}N). These stable isotope compositions are expressed in terms of delta values (δ) in permil (‰), i.e., parts per thousand differences from a standard. They express the proportion of an isotope that is in a sample as follows:

$$\delta \mathrm{D}_{\mathrm{VSMOW}} = \left(\frac{(\mathrm{D/H})_{\mathrm{sample}}}{(\mathrm{D/H})_{\mathrm{VSMOW}}} - 1 \right) \times 1000 \tag{1}$$

$$\delta^{17,18}\mathrm{O}_{\mathrm{VSMOW}} = \left(\frac{\left(^{17,18}\mathrm{O}/^{16}\mathrm{O}\right)_{\mathrm{sample}}}{\left(^{17,18}\mathrm{O}/^{16}\mathrm{O}\right)_{\mathrm{VSMOW}}} - 1 \right) \times 1000 \tag{2}$$

$$\delta^{15}\mathrm{N} = \left(\frac{\left(^{15}\mathrm{N}/^{14}\mathrm{N}\right)_{\mathrm{sample}}}{\left(^{15}\mathrm{N}/^{14}\mathrm{N}\right)_{\mathrm{standard}}} - 1 \right) \times 1000 \tag{3}$$

where $(\mathrm{D/H})_{\mathrm{VSMOW}}$ and $(^{17,18}\mathrm{O}/^{16}\mathrm{O})_{\mathrm{VSMOW}}$ are the isotope ratios of VSMOW (Vienna Standard Mean Ocean Water), generally used as the standard for water isotopic ratio.

The molecule behavior considerably depends on the isotopic properties, which can be divided into mass dependent and independent fractionation. In mass dependent fractionation, according to reaction kinetics, the delta value of isotopic species $^{m+\Delta m}\mathrm{X}$ for $^{m}\mathrm{X}$ at time t is obtained as:

$$d\left[^{m}\mathrm{X}\right] = -k_m \cdot \left[^{m}\mathrm{X}\right] \cdot dt \tag{4}$$

$$k_m \propto m^{-\alpha} \tag{5}$$

$$\therefore \ \delta^{m+\Delta m}\mathrm{X} = -2\alpha \frac{\Delta m}{m} \ln \left(\frac{\left[^{m}\mathrm{X}\right](t)}{\left[^{m}\mathrm{X}\right](0)} \right) \times 1000 \tag{6}$$

Therefore, the relative variations in isotopic ratios scale with the difference in mass of the isotopic species:

$$\frac{\delta^{m+2\Delta m}\mathrm{X}}{\delta^{m+\Delta m}\mathrm{X}} = 2 \tag{7}$$

2.2 Water isotopics

2.2.1 Origin of the Moon water

As plausible sources of Moon water, possibly contributing to the isotopic fractionation, two possibilities are mainly considered: (i) Hydrogen derived from the solar wind. Implanted protons from the solar wind would react with oxides in the lunar regolith and form OH/H_2O [8] [9]. The flux of protons on the Moon surface is estimated to be on the order of $10^7 \sim 10^8$ $cm^{-2}s^{-1}sr^{-1}$ [15], [16]. (ii) The micro meteorites with water components. These materials are considered to impact the Moon surface with an accretion rate of $(3.66 \pm 0.44) \times 10^6$ kg yr^{-1} [17]. Additionally, the contribution of comets or asteroids may be important, but it is not determined quantitatively yet. Furthermore, Terada et al. (2017) reported that biogenic terrestrial oxygen has been transported to the Moon by the Earth wind (at least 2.6×10^4 ions cm^{-2} s^{-1}) [25].

2.2.2 Source of water isotopic composition in solar system: hydrogen

When focusing on the hydrogen isotopes in lunar water, we especially need to consider the contribution by (i). The δD value of the proto-solar nebula is estimated to be -865.2 ± 32.1 ‰ from measurements of the Jupiter atmosphere and of (^{3}He+D)/H in the solar photosphere [18]. Therefore, if the contribution of the solar wind implantation is dominant, the hydrogen isotope ratio of the lunar water would be significantly D-depleted. The LRO data suggested that the hydrogen flux onto the surface of lunar polar craters reached $\sim 10^{11}$ $m^{-2}s^{-1}$ around the rim walls [19]. Further, δD value of -950 ‰ was obtained from grains in a lunar sample, which was considered to be due to hydrogen injected by solar wind [22].

In contrast, the D/H ratio of planetary and cometary components are higher and widely distributed around the value of the earth [18], which the δ D values are $0 \sim 1000$ ‰ and potentially still higher.

Thus, the hydrogen isotope ratio of lunar water will result in between the values of solar wind and comet. Hence, enough dynamic range is necessary to analyze hydrogen isotope. Hydrogen isotope ratio is easily fractionated because of the light atomic weight. Therefore, it is not appropriate to discuss the small difference of

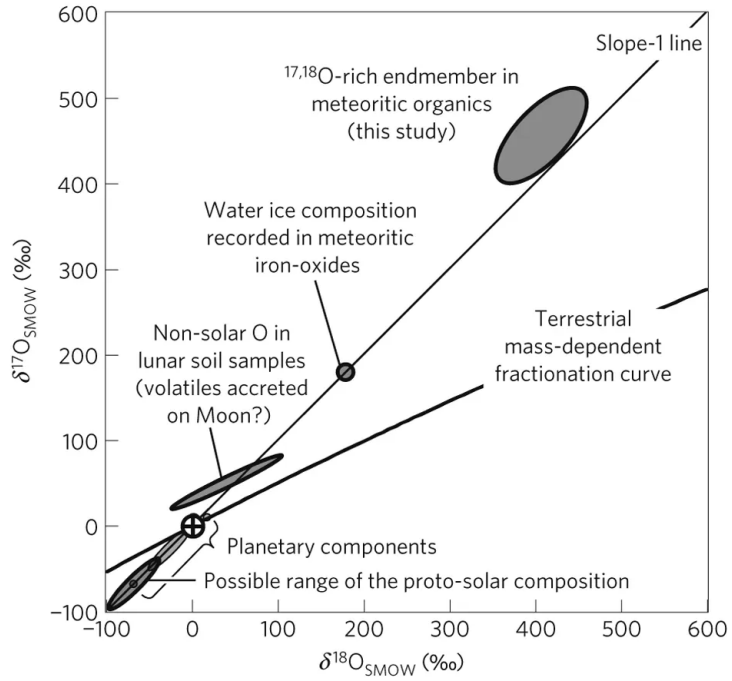

Figure 1 Oxygen isotopic distribution in planetary components. (Cited from [23])

δ. Required accuracy of δD of $\pm$ 100 ‰ is still reasonable to distinguish the solar wind effect on lunar water.

2.2.3 Source of water isotopic composition in solar system: Oxygen

The range of variation in oxygen isotope ratios is relatively smaller, but their distribution is more complicated because oxygen has three stable isotope species. In a δ^{17}O to δ^{18}O plot, the solar system materials show a trend along a 1-slope line. This is considered the result of mass independent fractionation by the mixing of components with different enrichment of ^{16}O during the formation of the solar system. While Δ^{17}O (δ^{17}O deviation from the terrestrial mass-dependent fractionation line, which the slope is $\sim$0.52) of the solar wind is less than -20 ± 4 ‰, Δ^{17} values of primitive chondrites are distributed between the solar fractionation line and the terrestrial fractionation line [21] [22]. Recently, ^{17,18}O-rich (up to 500 ‰) components have been discovered in meteoritic iron-oxides and organics, which are probably potential counterpart end members of the solar composition [23] [24].

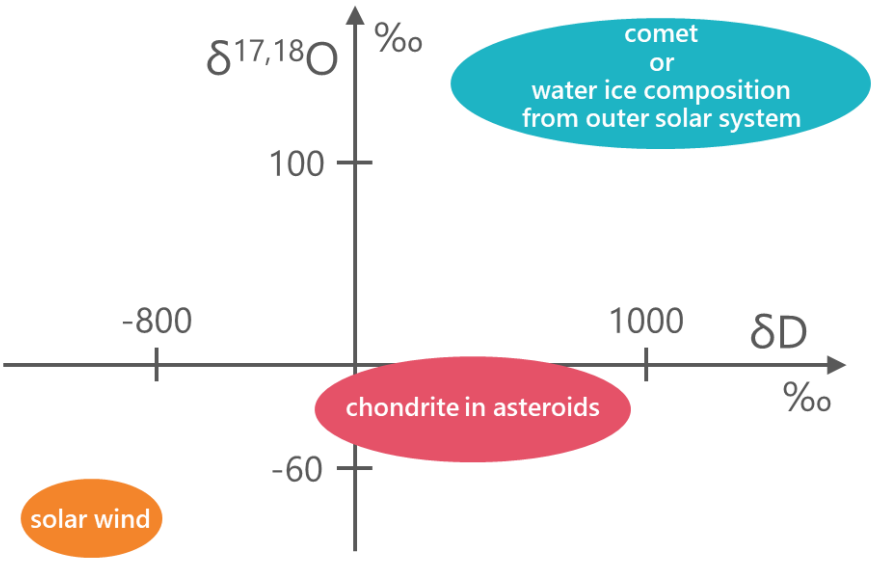

Figure 2 Distribution Diagram of $\delta^{17,18}$O and δD of components in the solar system.

Thus, taking previous research into consideration, we set the required accuracy of δD and $\delta^{17,18}$O for isotopic measurement of the lunar water at $\pm$ 100 ‰and $\pm$ 10 ‰, respectively.

2.3 Ammonia isotopics

2.3.1 Ammonia on the moon and in the solar system

Ammonia is a significant industrial and agricultural resource. Haber–Bosch process has been one of the most practical chemical reactions in a human history. Also, it is an important material in earth and planetary environment, especially as the raw material of various organic materials.

In 1972, the final space ship of t the Apollo mission (Apollo-17) with a humans crews was launched to the moon, and several pieces were sent for scientific observation. The Lunar Atmospheric Composition Experiment (LACE) was a mass spectrometer, a part of The Apollo Lunar Surface Experiments Package (ALSEP). It detected mainly Argon, Helium and also an slight amount of ammonia [27] [28].

In 2009, this time an unmanned spacecraft, The Lunar Crater Observation and Sensing Satellite (LCROSS) was sent to the moon. While it detected a sign of water in the soil in the Cabeus crater using IR spectroscopic method, also ammonia was observed in an abundance of 6.03 % relative to water.

In other cases of the inner region of the solar system, signatures of ammoniated

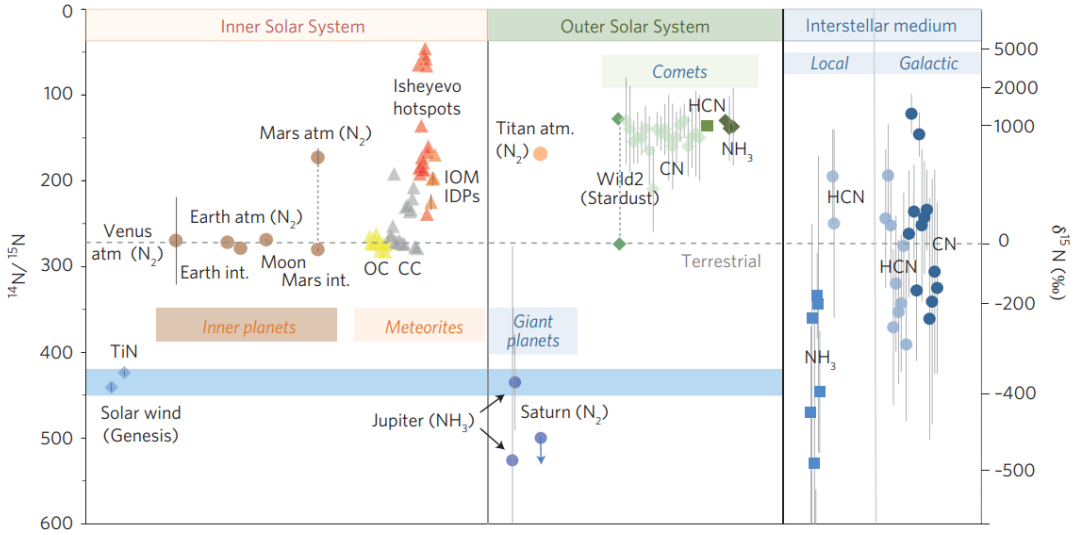

Figure 3 Nitrogen isotopic distribution in planetary components. (Cited from [35])

minerals were observed on the surface of a dwarf planet Ceres [29] [30] [31]. The origin of ammonia on the Ceres is controversial among scientists. Ceres might be carried after forming at a location where ammonia ices were stable, or might originate near the current location with an ammonia-rich environment [32].

The freezing point of ammonia is -77.7 °C, so ammonia is stable as a solid form beyond the outer side of the asteroid belt. In addition, ammonia readily dissolves in water, and has the effect of lowering the melting temperature of water ice [33]. This is an important property in a discussion of a subsurface ocean of icy moons. Cassini Orbiter, encountered a gas plume ejected from Enceladus in 2008, and detected ammonia at approximately 1 % in the water [34].

It's known that ammonia originating in the outer region of the solar system has a ^{15}N-rich isotopic ratio, especially in comets (δ^{15}N $\sim$ 1000 ‰), while nitrogen in the proto-solar nebula is estimated to be low (δ^{15}N = -375 $\pm$ 80 ‰) [35] [36] [37]. N_2 in Titan atmosphere is also ^{15}N-rich [38]. Considering the ranges of these isotopic ratio, we set the target value of precision in nitrogen isotopic ratios at least δ^{15}N $\pm$ 100 ‰.

2.3.2 Ammonia absorption lines in near-IR

The intensities of ammonia absorption lines are plotted in Figure 4. There are high intensity area around 1.5 μm, 2.0 μm, 2.3 μm and 3.0 μm. The empirical parameters of numerous $^{14}NH_3$ absorption lines are available in the HITRAN

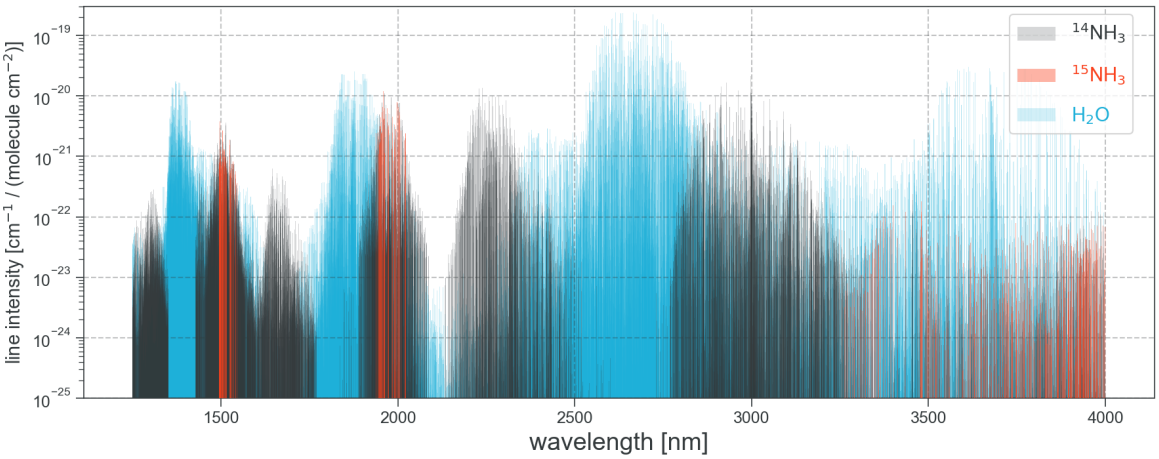

Figure 4 Line intensity S (cf. Equation 19) in near-IR. The $^{15}NH_3$ data around 1.5 μm are from B. Lins et al. (2010) [39], and others are from HITRAN database [41].

database [41], however, $^{15}NH_3$ data is not available in a wide range of near-IR region, except around 2.0 μm and above 3.3 μm. In a previous study, B. Lins et al. (2010) reported line intensities in a region around 1.5μm [39].

In the future exploration, it will be expected to measure ammonia-water ice. Therefore, a wavelength range including both absorption lines of water and ammonia will be better for a simultaneous observation. These molecules share the absorption areas around 1.5 μm, 2.5 μm, and above 3.5 μm.

2.4 Near-infrared absorption spectroscopy

Spectroscopy is the study of interaction of light and matter. When a molecule absorbs light with optical frequency ν, the energy of molecule is raised by $h\nu$ (h is the Planck constant). The increment of the energy corresponds to the energy levels of molecular vibration in the case of infrared (IR). Absorption wavelength and intensity depend on the species of the molecule, therefore we can get the matter-specific information from the absorption spectrum.

The vibrational energy $G(v)$ and the rotational energy $F(J)$ for gas phase molecules are described by

$$\begin{aligned} G\left(v\right) &= h\nu_n \left(v + \frac{1}{2}\right) \\ F\left(J\right) &= \frac{h^2}{2I} J\left(J+1\right) \end{aligned} \tag{8}$$

Then, the absorption energy $h\nu$ is given by

$$h\nu = G(v) + F(J) \tag{9}$$

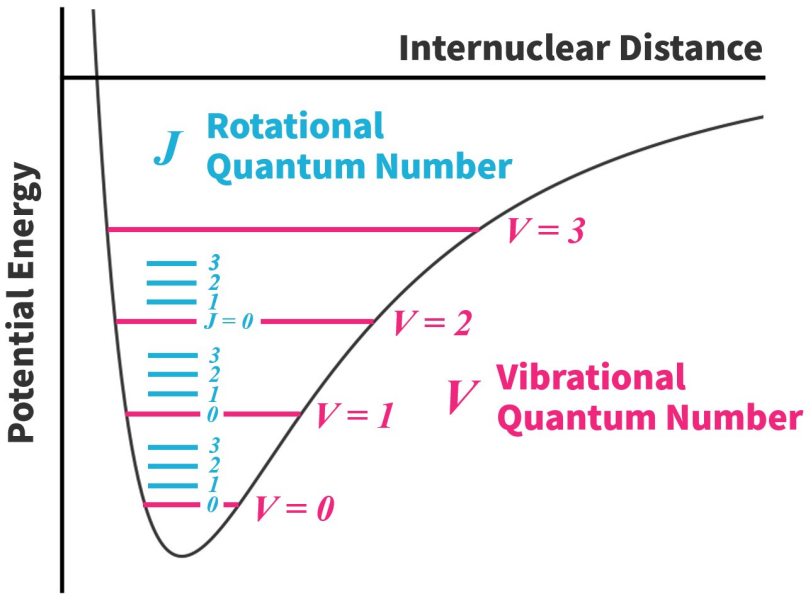

Figure 5 A schematic diagram of potential energy of a molecule.

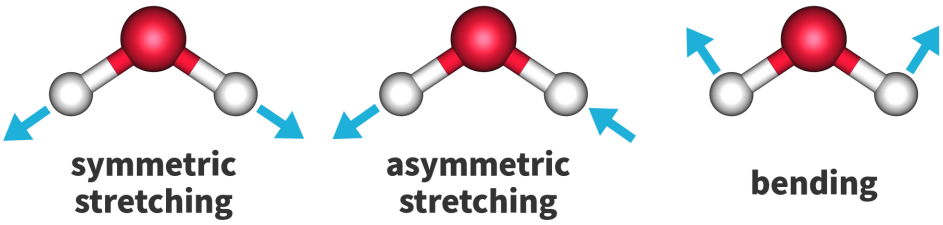

Figure 6 Normal vibration mode of a triatomic molecule.

where v and J are the quantum number of vibrational and rotational mode, ν_n and I are the normal mode frequency and the moment of inertia of the molecule, respectively.

A molecule generally has multiple normal modes. For example, H_2O molecule has three modes: symmetric stretching, asymmetric stretching and bending. As shown in Figure 6, transition occurs when the corresponding mode changes the dipole moment in the molecule. If the vibration is harmonic, transition only satisfying $\Delta v = \pm 1$ and $\Delta J = \pm 1$ is allowed. In higher energy region, typically corresponding to near-IR, the forbidden transition occurs because of anharmonicity of molecular vibration. This leads the overtone transitions in near-IR spectroscopy, although it is low intensity. This means low absorption coefficient, therefore near-IR spectroscopy useful for measurement that treats a long optical path length. Additionally, there are a lot of useful optical components for near-IR where have strong absorption lines of volatile molecule species (e.g., H_2O, NH_3, CO_2, CH_4 etc.).

2.5 Cavity ring-down spectroscopy

For on-site molecules observation in space mission, mass spectrometry (MS) methods were also generally employed. The history of onboard MS was started from 1960s, adopted Wien filter for mass selection. Types of time-of-flight and quadrupole mass spectrometer (QMS) are generally used in planetary exploration, which the mass resolutions M/ΔM reach 100. NASA's Mars Curiosity Rover loaded a QMS, and performed isotopic measurement of $^{40}Ar/^{36}Ar$ and $\delta^{13}C$ [13]. However, MS sometimes encounter a problem of mass resolution. For example, separation of ^{17}O and ^{16}OH, the mass of 16.9991 and 17.0027 respectively, require

$M/\Delta M > 5000$.

On other hand, absorption spectroscopy enables to measure a spectrum including an absorption peak of each molecule itself without destruction, while ionization with destruction is necessary in MS. In absorption spectroscopy, a peak separation is restricted by the temperature and the pressure, because these properties decide the broadening of absorption peak. Typically pressure lower than 10^3Pa is necessary to distinguish each peak of isotope species. This means isotopic measurement with spectroscopic method needs sensitivity in absorbance around $\sim 10^{-10}$.

Cavity ring-down spectroscopy (CRDS), also known as cavity ring-down laser absorption spectroscopy (CRLAS), is one of many types of laser absorption spectroscopy (LAS). Spatial coherence of laser light enables high collimation, yielding low light loss.

To increasing the path length, cavity enhanced absorption spectroscopy (CEAS) applies multi reflection system using a pair of high reflecting mirrors with the reflectivity better than 99.99%. Laser light forms multi-pass in the space between the mirrors, called "cavity", which contributes to increase interactions of laser light with molecules. Tunable diode laser absorption spectroscopy (TDLAS), a

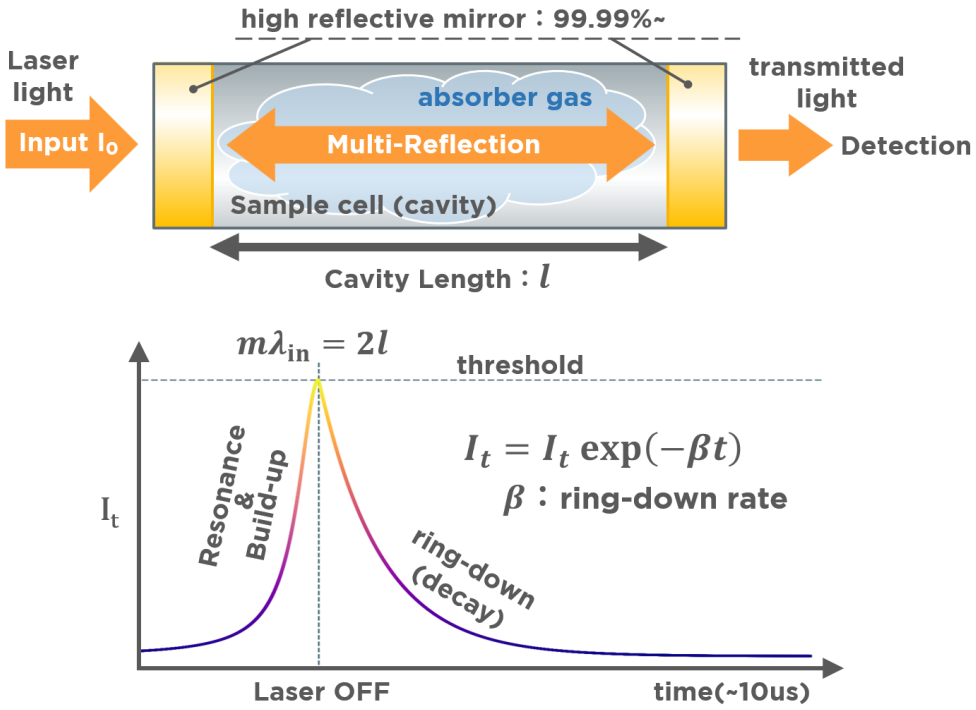

Figure 7 Schematic diagram of the principle of CRDS.

kind of CEAS, was also employed in Curiosity to measure the isotope ratio of water and carbon dioxide [14]. Integrated cavity output spectroscopy (ICOS), detecting integrated intensity behind one of the cavity mirrors, is a derivation of CEAS, which the sensitivity typically reaches $\sim 10^{-7}$.

In CRDS, the cavity works as a Fabry-Perot etalon. The light intensity is enhanced by optical interference when the laser wavelength and the cavity length satisfy

$$m\lambda_{\text{in}} = 2l \tag{10}$$

where m, λ_{in} and l are natural number, wavelength of input light and cavity length, respectively. The effective optical path length is defined as

$$L = \frac{l}{1-R} \tag{11}$$

where R is the reflectance of the each mirror. The typical L reaches to several kilometers. This feature enables CRDS to achieve the sensitivity above 10^{-10}.

The laser is turn off when the resonance conditions are satisfied, then the decay of transmitted light is detected. The decay rate depends on the conditions inside the cavity (e.g., gas species, abundance, pressure, temperature). Therefore, absorption properties of a gas sample can be obtained without detection of input light. The intensity of transmitted light is:

$$I_t(\nu) = I_0 \exp(-\beta t) = I_0 \exp\{-[\beta_0 - ck(\nu)]\, t\} \tag{12}$$

where c is speed of light. β is decay rate, also called ring-down rate. β_0 is the ring-down rate without absorber, which obtained as:

$$\beta_0 = \frac{c(1-R)}{l} \tag{13}$$

The optical frequency separation between intensity peaks of the transmitted light is called Free Spectral range (FSR).

$$\Delta\nu_{\text{FSR}} = \frac{c}{2l} \tag{14}$$

The full width half maximum (FWHM) of a single mode peak is obtained as

$$\Delta\nu_{\text{FWHM}} = \frac{c(1-R)}{2\pi l\sqrt{R}} \tag{15}$$

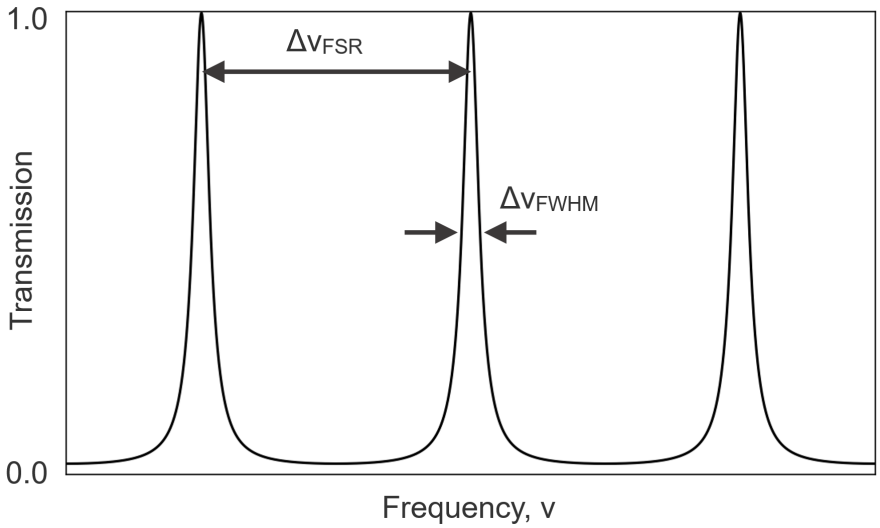

Figure 8 A schematic plot of a transmission from a Fabry-Perot etalon with chaniging the optical frequency.

This means that a Fabry-Perot etalon with higher reflectance mirrors has higher wavelength selectivity. This property allow a high wavelength resolution, while the relation between an intensity and a wavelength resolution are trade-off in continuous light spectroscopy. The finesse, a ration of FSR and the FWHM, is given by

$$F = \frac{\pi\sqrt{R}}{1-R} \tag{16}$$

As the reflectivity of the mirror approaches 1, the finesse increases, and the resonance becomes sharper.

2.6 Spectral calculation

When laser light I_0 passes an absorber gas with the optical path length L and the intensity of the transmitted light I_t, Beer's Law defines the absorbance α at optical frequency ν:

$$\alpha(\nu) = k(\nu) L = -\ln\left(\frac{I_t(\nu)}{I_0(\nu)}\right) \tag{17}$$

The absorption coefficient k including absorption transitions j of target molecule

species is obtained by:

$$\begin{aligned} k(\nu) &= \sum_{j,s} A_{j,s}\phi_j(\nu) \\ \int_{-\infty}^{\infty} \phi_j(\nu)\, d\nu &= 1 \end{aligned} \tag{18}$$

where $\phi_j(\nu)$ is a distribution function, determining the spectrum line profile. $A_{j,s}$, equals to the area of a spectral peak of the absorption transition, is given by:

$$A_{j,s} = S_j n \chi_s \tag{19}$$

where S_i is the line intensity of the transition. n and χ_s are the number density of the whole gas molecules and the fraction of the target molecule species, respectively. The total absorption is calculated by summation about all transitions j and species s in the target wavelength range (Equation 18).

As a line shape function, generally Lorentzian Profile (LP) f_L and Gaussian Profile (GP) f_G are took into account:

$$\begin{aligned} f_{\mathrm{LP}}(x) &= \frac{\gamma}{\pi(x^2+\gamma^2)} \\ f_{\mathrm{GP}}(x) &= \frac{1}{\sqrt{2\pi}\sigma}\exp\left(-\frac{x^2}{2\sigma^2}\right) \end{aligned} \tag{20}$$

LP is explained by broadening derived from molecular collision, the HWHM γ approximately proportional to p/T^n, where p is the partial pressure of the molecule species, T is the temperature and n is the dependency coefficient. On the other hand, GP is explained by broadening derived from Doppler effect depending on the distribution of molecules velocity, the HWHM σ is obtained by $\nu_{0,j}\sqrt{k_B T/mc^2}$, where $\nu_{0,j}$, k_B, m and c are optical frequency at the transition in vacuum, Boltzmann constant, the molecular mass and the speed of light, respectively.

Voigt Profile (VP), defined as a convolution of f_{LP} and f_{GP} is useful to account for the spectral line shape because of the computational simplicity:

$$\begin{aligned} & f_{\mathrm{VP}}(x) = \int_{-\infty}^{\infty} f_L(x-t)\, f_G(t)\, dt \\ \therefore\ & f_{\mathrm{VP}}(\nu-\nu_{0,j}) = \frac{1}{\sqrt{2}\pi^{3/2}}\frac{a}{\sigma}\int_{-\infty}^{\infty}\frac{e^{y^2}}{(x'-y)-a^2}dy \\ & a = \gamma/\sqrt{2}\sigma, \quad x' = (\nu-\nu_{0,j})/\sqrt{2}\sigma \end{aligned} \tag{21}$$

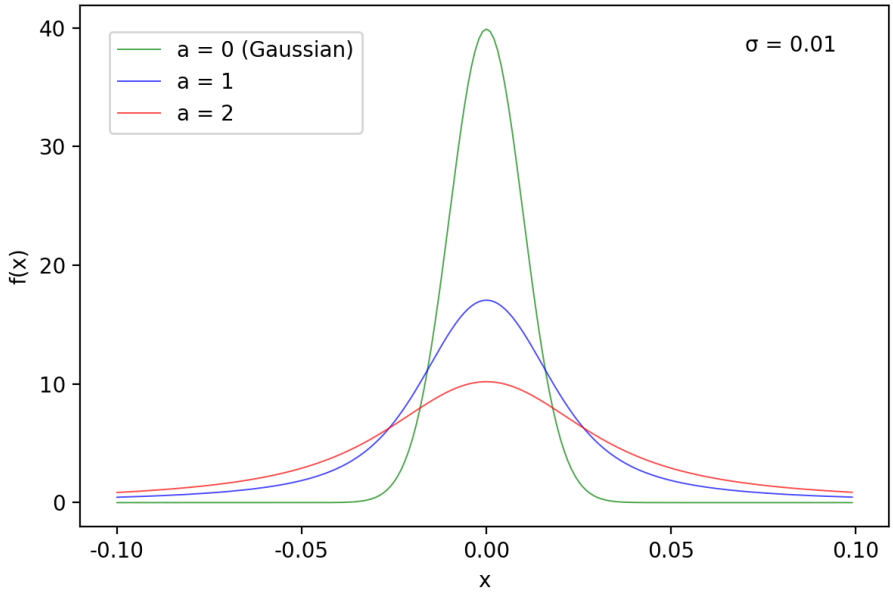

Figure 9 Voigt function plot at σ of 0.01. Voigt function get close to Gaussian function as the a approaches to 0.

Although above equations cannot be calculated analytically, approximate equations with the error function is available:

$$\begin{aligned} f_{\mathrm{VP}}\left(\nu-\nu_{0,j}\right) &\approx \frac{\mathrm{Re}\left[e^{-z^2}\mathrm{erfc}\left(-iz\right)\right]}{\sigma\sqrt{2\pi}} \\ z &= \frac{\nu-\nu_{0,j}+i\gamma}{\sigma\sqrt{2}} \end{aligned} \tag{22}$$

Thus, α is expressed as:

$$\begin{aligned} \alpha\left(\nu\right) &= \frac{PL}{k_BT}\frac{1}{\sigma\sqrt{2}\pi}\sum_{j,sp} S_j\chi_{sp}\mathrm{Re}\left[e^{-z_j^2}\mathrm{erfc}\left(-iz_j\right)\right] \\ z_j &= \frac{\nu-\nu_{0,j}+i\gamma}{\sigma\sqrt{2}} \end{aligned} \tag{23}$$

Thus, when we get spectrum including transition line $j = 1, 2$, for example, corresponding to the isotopic species HHO and HDO, the isotope ratio in a sample R_{sample} is obtained as

$$R_{\mathrm{sample}} \sim \frac{\chi_{\mathrm{HDO}}}{\chi_{\mathrm{HHO}}} = \frac{S_{1,\mathrm{HHO}}A_2}{S_{2,\mathrm{HDO}}A_1} \tag{24}$$

Given an average value for isotope ratio as R_0, a delta value δD was defined as

$$\delta\mathrm{D}_{\mathrm{CRDS}} = \left(\frac{R}{R_0}-1\right)\times 1000 \tag{25}$$

3 D-depleted water isotopic measurement with a miniaturized CRDS with 5 cm cavity aiming for exploration of lunar water

3.1 Method

3.1.1 Apparatus

The mini-CRDS with a 5cm cavity was firstly developed in a study of Space-hub research (2016 - 2019) organized by JAXA. H. Abe et al. (2021) already reported a performance of the mini-CRDS as a moisture sensor for the trace level of water at atmospheric pressure [26]. The moisture detection limit of 3.1 ppb was obtained in nitrogen gas of 1 atm, which is less than 1 ng of water in the 15 cm^3 cavity. In this study, we focused on isotopic measurements, especially for HDO, using another model of mini-CRDS. The mini-CRDS used in this study is shown in Figure 10 and Figure 11. The mirrors (Japan Aviation Electronics Industry) had 99.9965 % reflectance, which yields the long effective optical path length (calculated as $L/(1-R)$ where L is cavity length and R is mirror reflectance) of 1.4 km with the cavity of 5 cm in length.

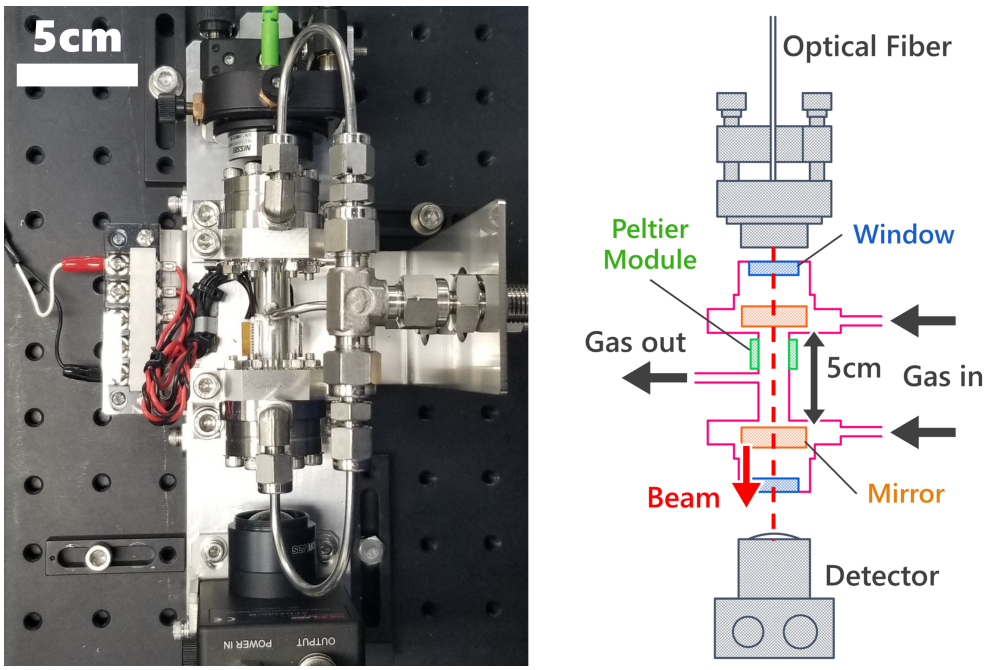

Figure 10 Photo (a) and illustration (b) of the mini-CRDS.

As the most conspicuous feature, the body of the mini-CRDS sensor was smaller than almost all the commercially available CRDS devices. The cavity with 5 cm length, optical fiber mount (5-Axis Kinematic Mount; K5X1, Thorlabs) and the avalanche photo detector (APD430C/M, Thorlabs) were fixed on an aluminum base plate rigidly. Laser light was introduced to the cavity from a fiber coupled distributed feedback (DFB) laser (NLK1E5EAAA, NTT Electronics). The wavelength of the laser light was enabled to scan 1360 nm to 1460nm with a current controller (LDC202C, Thorlabs) and a temperature controller (TED200C, Thorlabs). To obtain an absorption spectrum, wavelength of the laser light was scanned over the range of approximately 7185.72 cm^{-1} to 7186.38 cm^{-1} by a reverse sawtooth wave function at 10Hz, which was used as tuning signal of the laser. The deviation from linearity on the wavenumber against the turning signal was less than 2%. The signal from the photo detector was sent to a trigger unit and an A/D converter (16 bit and 25MHz, TUSB-0216ADMH, turtle industry). The trigger unit turned off the laser diode when the signal intensity exceeds a threshold. The ring-down signals and the tuning signals of laser are simultaneously recorded and ring-down signal was fitted by an exponential function, then the ring-down rate was estimated.

In isotopic spectroscopy, it is necessary to distinguish adjacent peaks in an absorption spectrum. Therefore, measurement at low pressure ($<$ 100 Pa) was performed to obtain a condition of narrow absorption line width. The both ends of the cavity were sealed by ICF flanges with windows, and the cavity was connected to a preparation chamber via valves. The whole system was able to be evacuated using a rotary pump up to $<$ 1Pa. Before introducing into the cavity, sample gas was stored in a chamber that has a volume of 1000 cm^3. Since the volume of the cavity was 15 cm^3, 1.5 % of the whole gas was introduced to the CRDS cavity.

Peltier element modules attached on the outer surface of the cavity were used to control the cavity length by the thermal expansion. As illustrated in Figure 12, FSR of 5 cm cavity does not have enough resolution to measure a narrow absorption spectrum. In order to interpolate the gaps of FSR, it is necessary to change the cavity length. The Peltier element modules were driven at 5 V and repeatedly switched at $\pm$ 200 mA with an interval of 10 seconds. Considering the thermal expansion coefficient of steel (SUS-304) of 17×10^{-6} (1 /°C), $\pm$ 0.4 °C temperature change is required to interpolate the gaps completely. Generally, Piezoelectric element (PZT) is used to change the optical length in CRDS. The

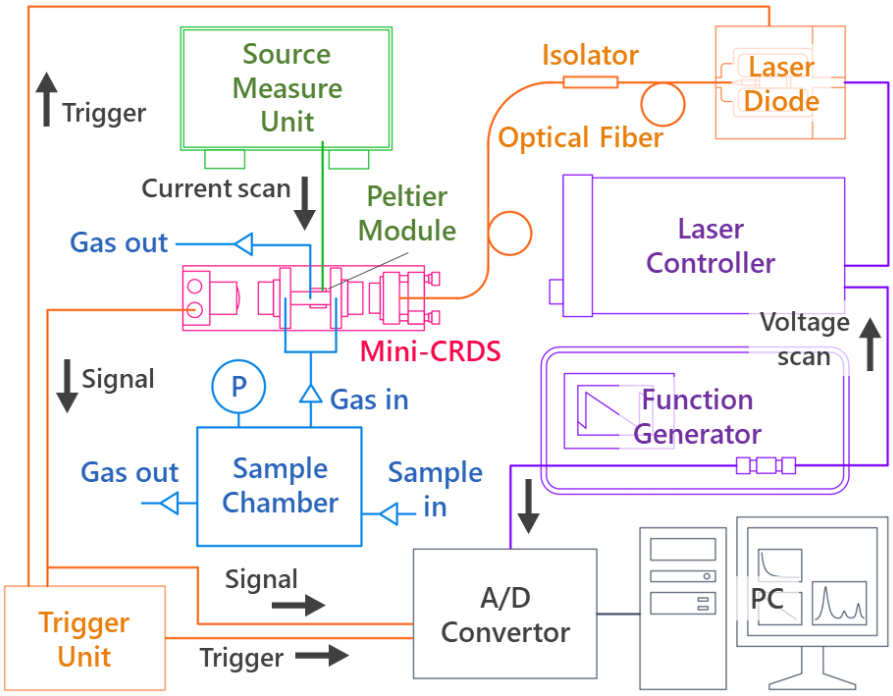

Figure 11 Illustration of peripheral equipment. Ⓟ represents a pressure gage. All gas outs were connected to a vacuum pump.

advantage of the PZT is the easy and quick control but the mechanical structure is necessary. On the other hand, the advantage of Peltier modules is the simple structure, which can be attached additionally to the cavity surface. It will result in a robust optical alignment under the severe vibration supposed at launching of a rocket.

3.1.2 Experiment

In this study, our aim is to determine a calibration line of D/H ratio using the mini-CRDS. Before such experiments, we must estimate the influence of the "sample-memory effect", which means the effect of the previous residual sample on the next. This effect has a serious influence on isotopic measurement. We measured the remaining water in the mini-CRDS cavity during evacuation, using an absorption line at 7178.45 cm^{-1} with the line intensity of 1.44×10^{-22} $\mathrm{cm}^{-1}/(\mathrm{molecule} \cdot \mathrm{cm}^{-2})$. First, the water sample of 100 Pa was introduced to the cavity through the sample chamber appearing in Figure 11. After one hour, evacuation of the cavity was started. Then, the change in absorption spectrum

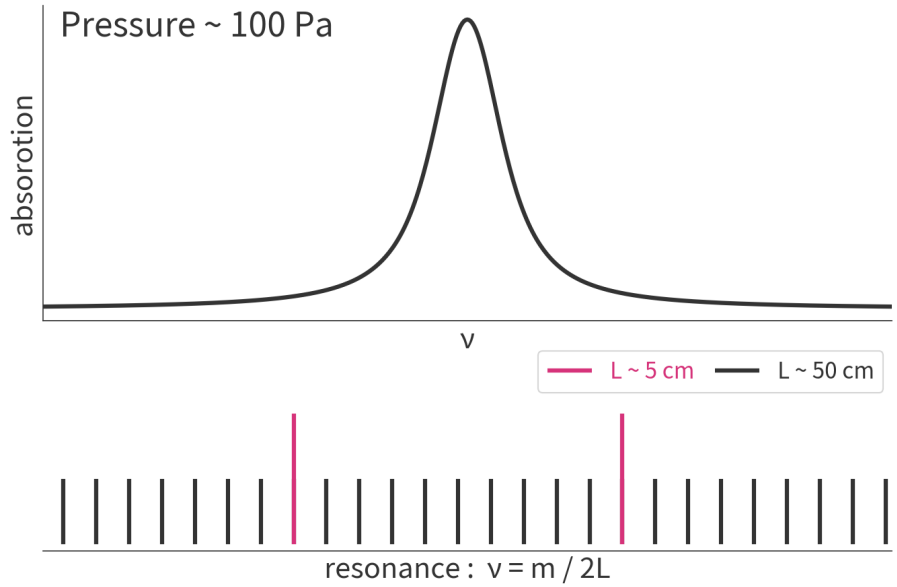

Figure 12 A schematic diagram of comparison between an absorption spectrum and FSR for 5 cm and 50 cm cavity. Water vapor pressure of 100 Pa is assumed. Resonance wavenumber satisfies $\nu = m/2L$ where m is natural number.

sample No.	$\delta D_{\mathrm{VSMOW}}$ (‰)
1	-188.8 ± 1.0
2	-143.1 ± 1.0
3	0.082 ± 1.0
4	160.9 ± 1.0
5	479.3 ± 1.0
6	-987 ± 19

Table 1 D/H ratios of the water standard samples.

was measured during the evacuation (Figure 13). The decay curve of the water amount could be explained with a function including fast and slow components of exponential. These could be decrement of the water vapor in the cavity space and molecules adsorbed on the cavity surface, respectively. It took around 60 minutes to reduce the water amount to 5%. According to the required accuracy of $\sim 10\%$, the evacuation time before starting each measurement was set to 60 minutes or longer.

To determine the calibration line of the D/H ratio, we performed measurements of 6 water standard samples with different $\delta \mathrm{D}_{\mathrm{VSMOW}}$. All the samples were already

measured using a mass spectrometer by Shoko Science Co. The known δD_{VSMOW} values of the samples are shown in Table 1. In all measurements, 10 μL of sample water was vaporized in the chamber before introducing into the cavity, and then the pressure was adjusted to 100 Pa. β was measured 2000 times for a single spectrum (Figure 14), and an average of 15 spectra were used for determining a conclusive D/H ratio. The measured spectra were fitted with the Voigt profile and δD_{CRDS} was calculated according to the process mentioned in section 3.

3.2 Result and discussion

3.2.1 Absorption spectrum

The wavelength range in this measurement includes three absorption lines of S>10^{-25}, shown in Figure 14, where peak-1, -2 and -3 correspond to 7184.10 cm^{-1} ($HH^{16}O$), 7183.97 cm^{-1} ($HD^{16}O$) and 7183.88 cm^{-1} ($HH^{16}O$) respectively. In addition, these three absorption lines were influenced by the tail of an intense line of $HH^{16}O$ at 7182.95 cm^{-1}, with the line intensity being 3.77×10^{-21} $cm^{-1}/(molecule \cdot cm^{-2})$. We used a quadratic function to evaluate this tail. This allows a reduction

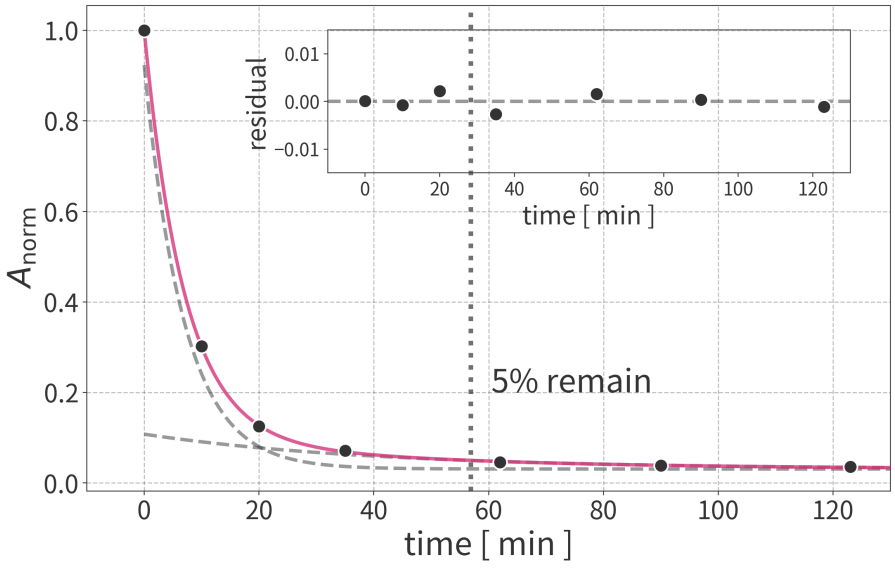

Figure 13 Decay plot of residual water in the cavity during evacuation. A_{norm} is the spectrum area of absorption line at 7178.44 cm^{-1}, normalized by the value of time = 0. The red line is a fitted function including two components of exponential (broken lines).

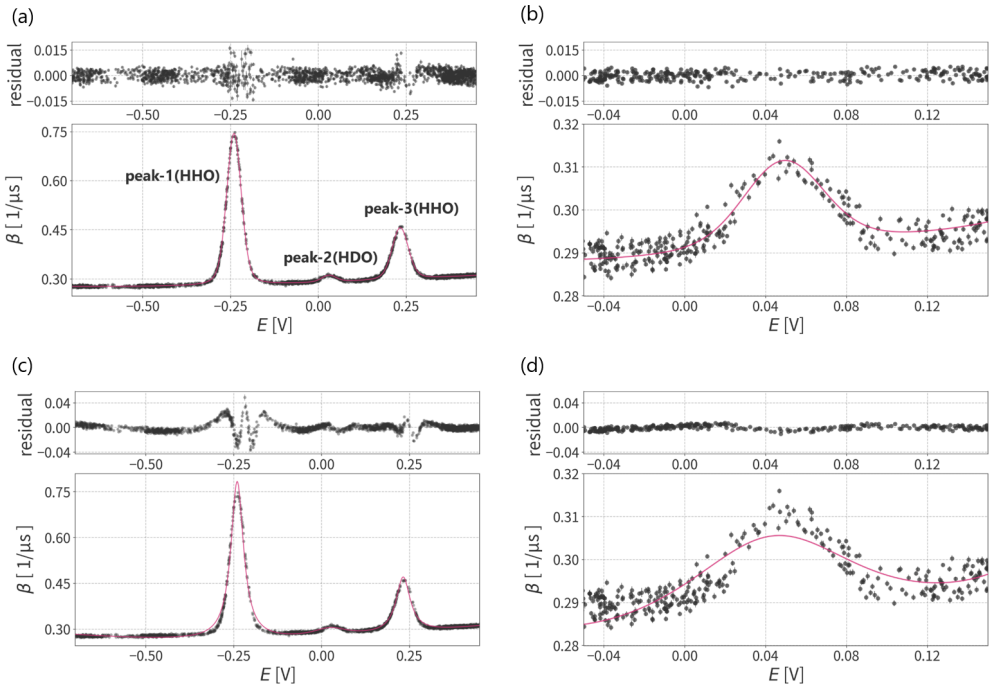

Figure 14 (a) A spectrum of sample-6 with Voigt profile fitting. (b) the enlarged view of peak-2 in (a). (c) The same spectrum as (a) with Lorentzian profile. Horizontal axis E is the voltage output from a function generator that controls the laser wavelength, corresponding the range of approximately 7185.72 cm^{-1} to 7186.38 cm^{-1}. Peak-1, 2 and 3 correspond to absorption lines that each the center is 7184.10 cm^{-1}, 7183.97 cm^{-1} and 7183.88 cm^{-1} respectively. Wavelength notations are adopted for the HITRAN database[41].

int the number of parameters compared to the Lorentzian. Reduction of the freedom degree of a fitting model is important to prevent over-fitting. In the condition of this measurement, at a low vapor pressure of 100Pa, Lorentzian profile does not fit as shown in Figure 14 (c) & (d). That is because broadening by collisions between molecules in a gas is not dominant in this pressure range but due to Doppler effect caused by velocities of the water molecules, or mixture of these mechanisms.

3.2.2 Hydrogen Isotopic ratios

The comparison and calibration line between the measured and known δD is shown in Figure 15 (a). Each δD_{CRDS} was calculated assuming the R of sample-3 equals to R_0 (cf., Equation 25). Because the wavelength range in this measurement

includes two HHO absorption lines (peak-1 and peak-3 in Figure 14), we got two δD_{CRDS} values from peak-2/peak-1 and peak-2/peak-3 for a sample. However, there were a few differences between them. The calibration lines between δD_{CRDS} and δD_{VSMOW} were calculated by linear least squares fitting. The R-squared of the calibration lines were 0.986 for peak-2/peak-1 and 0.981 for peak-2/peak-3.

The systematic error in the slope coefficient and the variance of δD_{CRDS} from the calibration lines were possibly caused by instability of the room temperature. Line intensity includes temperature as the parameter of a function, so the calibration line would shift if the temperature changed. Figure 15 (b) shows the calculated δD deviation from the calibration line of δD_{CRDS} using peak-2/peak-1, as a function of temperature change. The δD shift caused by temperature change is non-parallel to the calibration line because the HDO absorption line at 7183.97 cm^{-1} is more sensitive to temperature than the HHO line at 7184.10 cm^{-1}. As shown in Figure 15 (b), The variance of the δD can be explained by approximately ± 1 °C change of temperature. Although the temperature change by the Peltier element modules was estimated as ± 0.4 °C, but such variation would be averaged over the measuring

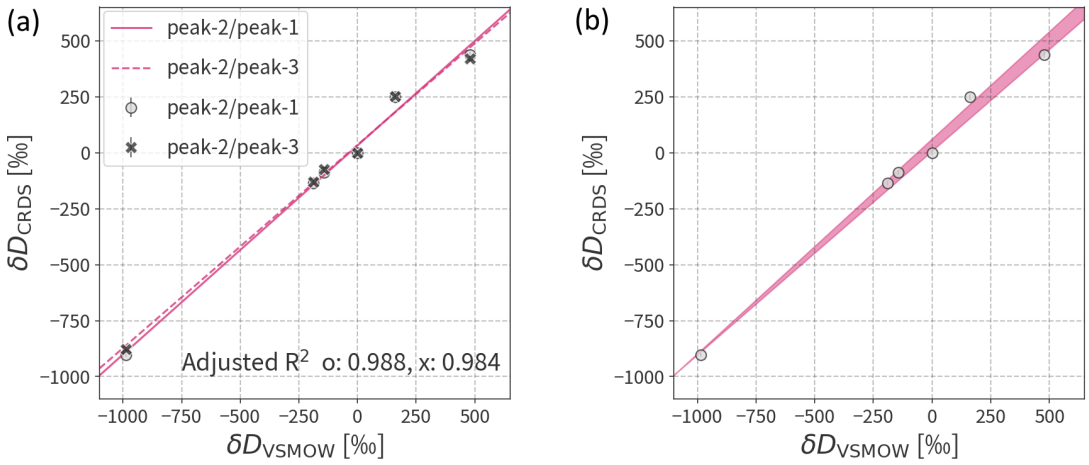

Figure 15 (a) Calibration plots with water standard samples measured using the mini-CRDS. The horizontal axis is the known δD_{VSMOW} of samples shown in Table 1. The D/H ratio of sample-3 was used as the R_0 of δD_{CRDS} in Equation (25). The circle and cross symbol represent results from peak2/peak1 and peak2/peak3 respectively. The solid and broken line represent fitted lines of peak-2/peak-1 and peak-2/peak-3 respectively. All lines were obtained by linear regression with least squares. (b) Calculated δD deviation from the calibration line in (a) using peak-2 / peak-1, as a function of temperature change. The red region indicate deviation with a range of ± 1 °C.

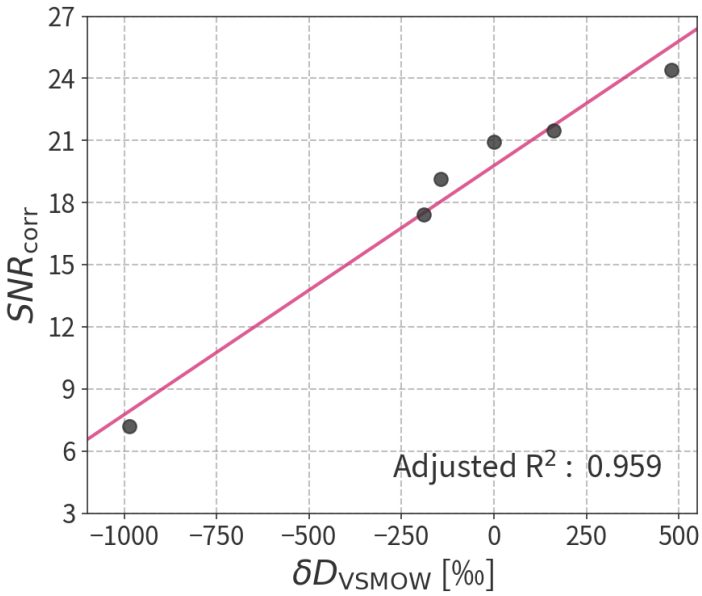

Figure 16 Corrected SNR of peak-2. The red line was obtained by linear regression with least squares.

time. While, room temperature change in the series of measurements was slow and as high as 5 °C, so that the systematic error appearing in the calibration line is strongly affected by the room temperature change.

3.2.3 Signal-to-noise ratio

Finally, we estimated the signal-to-noise ratio (SNR) of each sample for peak-2. The SNR obtained from a single spectrum was calculated by

$$\mathrm{SNR} = \frac{H_{\mathrm{peak2}}}{\sigma_{\mathrm{noise}}} \tag{26}$$

where H_{peak2} is the peak-2 height. σ_{noise} is a standard deviation of the spectrum noise. the noise corresponds to the residual of the measured spectrum after subtracted by the fitted Voigt profile. Here, corrected SNR is defined as:

$$\mathrm{SNR}_{\mathrm{corr}} \equiv \mathrm{SNR}_{\mathrm{mean}} \frac{A_{\mathrm{meanAll}}}{A_{\mathrm{mean}}} \tag{27}$$

$\mathrm{SNR}_{\mathrm{mean}}$ is the mean of SNR for the 15 spectra measured for each sample. A_{mean} is the mean of peak-1 area for the 15 spectra. Then, A_{meanAll} is the average of A_{mean} for all 6 samples. The correlation between $\mathrm{SNR}_{\mathrm{corr}}$ and $\delta\mathrm{D}_{\mathrm{VSMOW}}$ is shown in Figure 16. $\mathrm{SNR}_{\mathrm{corr}}$ for sample-6 was 7.17, which 3 is generally supposed as

the detection limit. The adjusted R^2 of the fitted line in Figure 16 was 0.959. Therefore, those SNRs were plotted nearly on the linear trend, indicating the noise was constant through measurements and had little effect on spectrum fitting. Thus, we can conclude the mini-CRDS has the ability to measure a D-depleted sample with δD_{VSMOW} as low as -980 ‰ without disturbance of the noise.

3.2.4 Oxygen isotopes

Additionaly we investigated oxygen isotopes. It was more difficult than the case of Hydrogen isotopes, because we needed to seek spectral region including absorption lines of three species, $H_2^{16}O$, $H_2^{17}O$ and $H_2^{18}O$.

We measured sample-3 with the laser wavelength range near 1390nm (Figure 17 (a)). The measurement equipment and condition were the same as the measurement of Hydrogen, mentioned above. This region included the whole species we would like to look. However, a tail of a huge peak (Peak-9) interfered over the measurement range. It was difficult to approximate the spectral profile of all absorption peaks at once, therefore we divided the measured spectrum into two pieces—spectrum-A including Peak-1∼6 and spectrum-B including Peak-7∼9. Spectrum-B were influenced by a another huge peak (peak-10) located in the outer region. Spectrum-A were primary fitted, then spectrum-B was subtracted by the fitted profile of spectrum-A (Figure 17 (b) & (c)). We measured the spectrum and repeated on the same sample over ten times. The pair plots of the estimated δ values of sample-3 were shown in Figure 18. These δ values were calculated with the standard values same as the average ratio. These values distributed over a range of 40% with anomalies which. This anomalies likely to derived from the data points measured when the sample was just after injected. Similar trends were observed also in the Hydrogen and Ammonia isotopic measurements. If these anomalies are excluded as the experimental biased data, though the variance of Δ^{17} don't satisfy the required accuracy of ¡ 10 ‰ , we can recognize a correlation likely derived from mass dependent fractionation between those values.

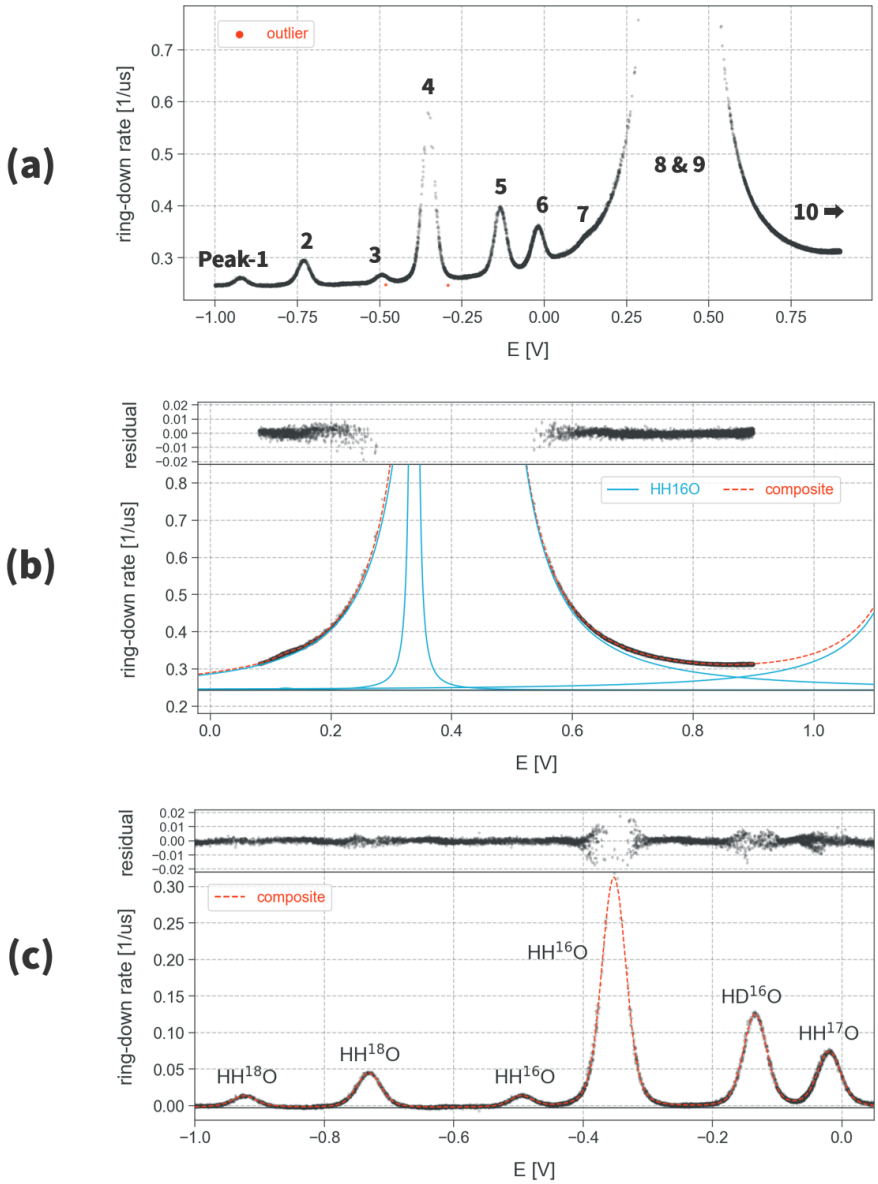

Figure 17 (a) Raw measured spectrum including absorption peaks of Oxygen isotopic water molecules. Horizontal axis E is the voltage output from a function generator that controls the laser wavelength, corresponding the range of approximately 1390.52nm $\sim$ 1390.78nm. This region includes ten detectable absorption peaks. (b) Spectrum-B, including Peak-7$\sim$9. Blue lines represent the fitted profiles of individual absorption peaks, and a red broken line represents the composite profile. (c) Spectrum-A, including Peak-1$\sim$6. It was subtracted by the composite profile of Spectrum-B. A black line equals the subtracted tail line of Peak-9. A red broken line represents the composite profile.

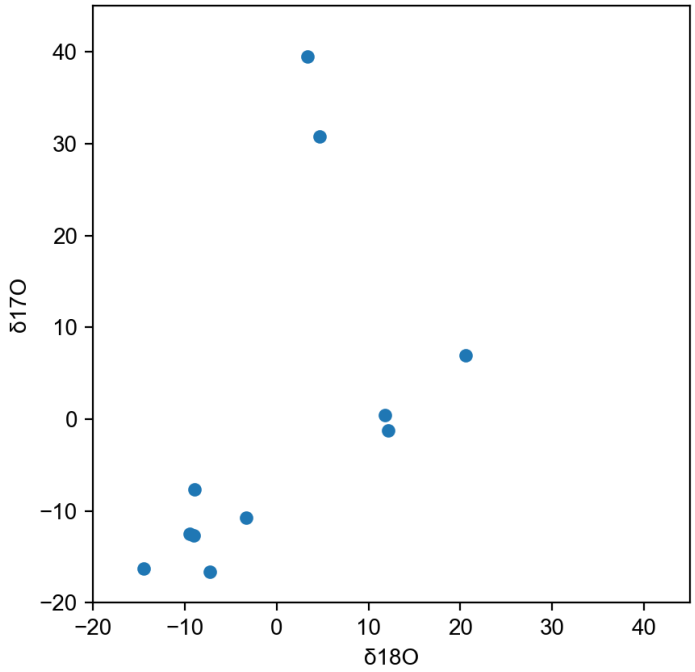

Figure 18 Plot of delta values as the result of sample-3 measurement. These values were calculated with the standard values same as the average ratio.

3.3 Conclusion

In this study, we show the measurement of D-depleted water isotopic measurement using a mini-CRDS with a cavity of 5cm in length. Six standard water samples, one of which was D-depleted $\sim$ -987 $\pm$ 19 ‰, were successfully measured, and the D/H ratios were analyzed by Voigt profile fitting. We obtained the calibration lines by comparison between measured and known values, and it showed enough agreement to distinguish $\pm$ 100 ‰which is the required accuracy for hydrogen isotope measurement. In addition, we also obtained SNR for a HDO absorption peak. Although the calibration lines included a systematic error and an influence from ambient temperature change, the SNR for the most D-depleted sample was 7.17 enough higher than the detection limit of 3.

While we adopted the Peltier module to tune the cavity length and it worked well, we will able to choose a piezoelectric module for more precise and quick resonance control. It will be a trade-off between robustness and functionality.

We also challenged Oxygen isotopic measurement. We have yet to achieve the required accuracy of ± 10 ‰because of the difficulty in the analysis of the spectrum. However, we obtained the spectrum including the all oxygen isotopes successfully, and confirmed that our CRDS can recognized at least the trend of mass-dependent fractionation. In the future study, we need to develop an analysis method robuster against the noise and the peak interference, or need to change the wavelength range(for example 2.7 μm) and search absorption lines easier to measure. Above all, the mini-CRDS in this study achieved remarkable downsizing as a high-sensitive isotope measuring method. CRDS will be a useful choice for mobile and in-situ measurement, not only for a lunar mission, but for every Earth and planetary exploration.

4 Ammonia isotopic measurement of using CRDS with 1.5 μm DFB-laser

4.1 Apparatus

To specify the wavelength range of the light source, we first studied about absorption line intensities (Look at Section 2.3.2). Taking the availability of apparatus components into consideration, we selected wavelength region around 1495 nm for this study. The several examples of available mirrors around 1.4 and 1.5 μm are summarized in Table 2. Also, the DFB-lasers of 1.4 and 1.5 μm have been well developed because they are popular bands in optical communication. Figure 21 shows line intensities around 1495 nm, corresponding to the tunable zone with the laser package used in this measurement. Our CRDS system for ammonia isotopic measurement consists of a 1.5μm DFB-laser (NLK1S5EAAA, NTT Electronics) with a tunable wavelength range is 1494 $\sim$ 1496 nm, a 50 cm cavity made of stainless steel, 99.995 % reflectance mirrors (Coastline Optics) and

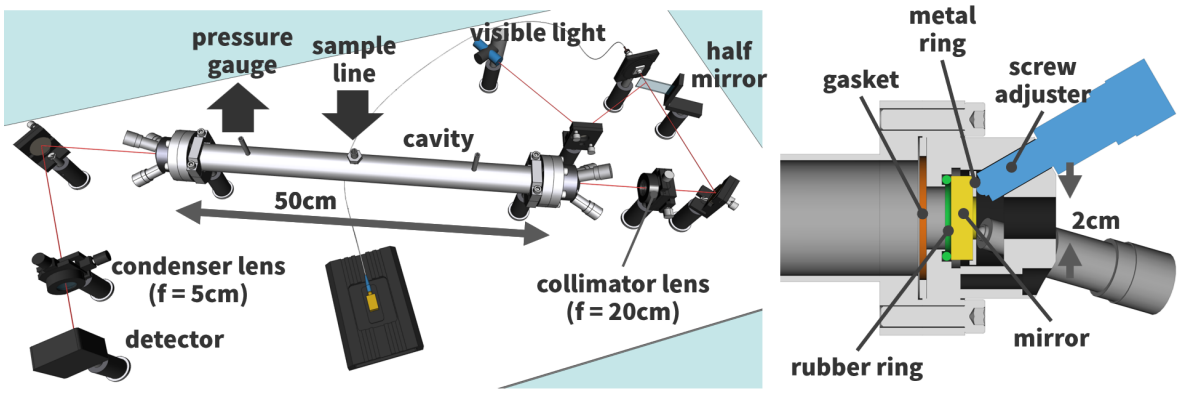

Figure 19 (a) Alignment of the 1.5μm-CRDS. (b) A cross section of the mirror mount of cavity.

manufacture	wavelength [nm] at reflectance >99.99 %
CRD Optics	1360 $\sim$ 1420
CRD Optics	1450 $\sim$ 1650
LohnStar Optics	1380 $\sim$ 1680
Layertec	1290 $\sim$ 1480

Table 2 The summery of available mirrors around 1.4 and 1.5 μm.

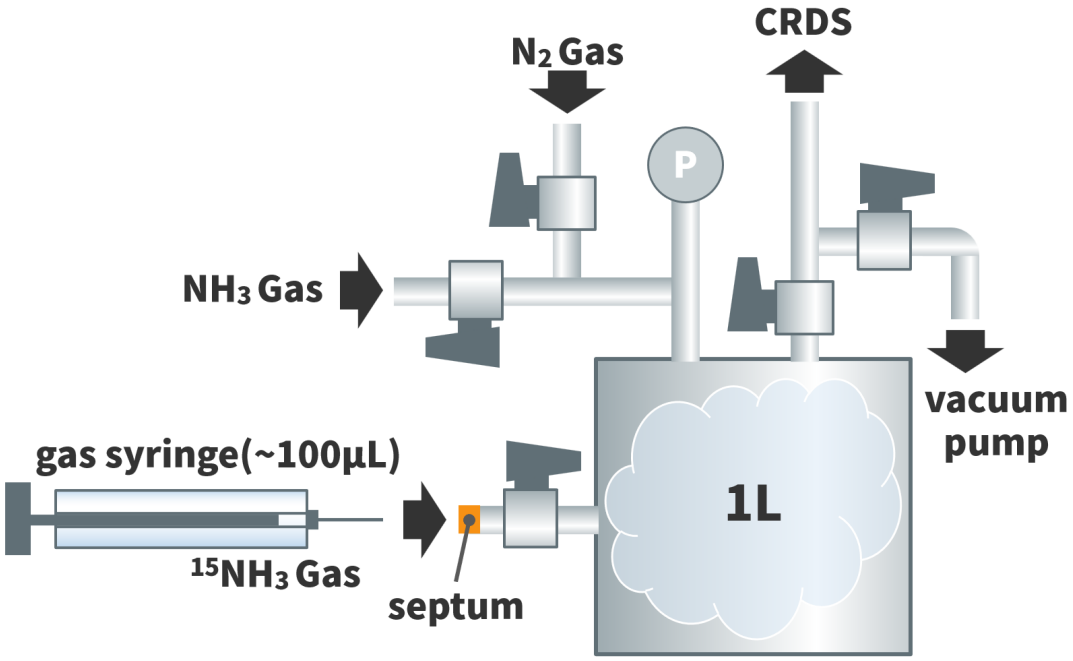

Figure 20 Schematic diagram of sample line. Ⓟ represents a pressure gage.

an InGaAs avalanche photo detector(APD430C, Thorlabs). All the system was built and fixed on an anti-vibration breadboard (FBS-86, Herz). The principle of trigger, wavelength tuning and signal acquisition were the same as Section 3. The difference is a delayed pulse generator (DG535, Stanford Research Systems) employed as a trigger unit.

As illustrated in 19(b), each mirror was fixed on a rubber o-ring with three-axis screw adjusters. The mirror mount was connected to a cavity tube by ICF flange with 70 mm diameter. The cavity tube, in which water repellent finish was applied on the inside, was 35mm in diameter and 50cm in length, so the volume was 480 cm^3. A belt heater was wound onto the cavity, and its temperature was controlled around 30 °C. This also plays a role in changing the cavity length to interpolate the gaps of FSR.

Figure 20 is an illustration of the sample line. NH_3 gas and N_2 gas were introduced to a 1L tank from compressed gas cylinders. Whole the system including CRDS was able to be evacuated up to 0.5Pa. To make variable mixtures of $^{14}NH_3$ and $^{15}NH_3$, 98 % $^{15}NH_3$ standard gas was introduced through a septum from gas syringe (up to 100 μL, 1710 Gastight Syringe, Hamilton co.). The specifications of these gas samples were summarized in table 3.

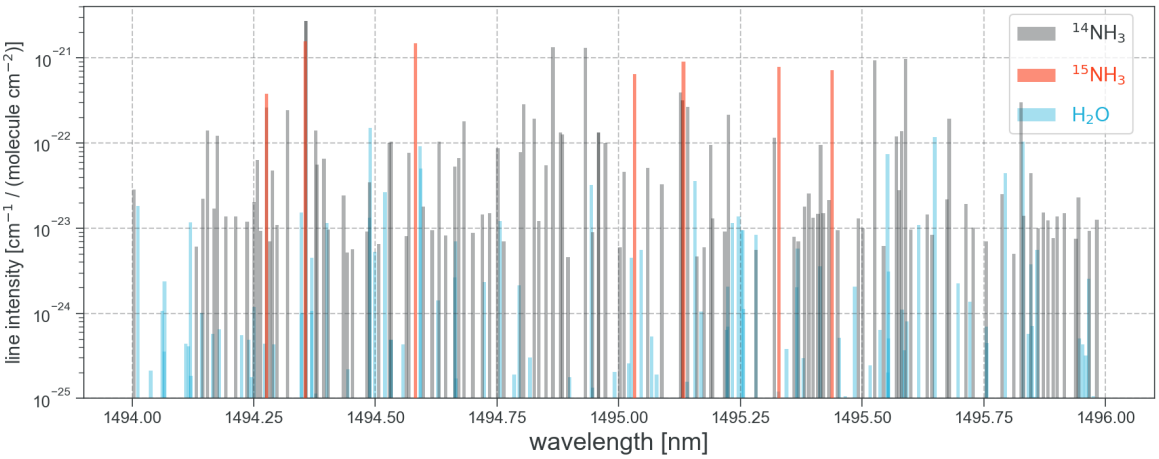

Figure 21 Line intensity S (cf. Equation 19) in an area around 1495 nm, which corresponds to the tunable area with the setup in this measurement. The $^{15}NH_3$ data are from B. Lins et al. (2010) [39], and others are from HITRAN database [41].

	content	purity
NH_3 gas	mixture of $^{14}NH_3$ and $^{15}NH_3$	99.9 %
$^{15}NH_3$ standard gas	98 % $^{15}NH_3$	$\geq$ 98 %
N_2 gas	N_2	99.999 %

Table 3 Summary of gas samples used in this measurement.

4.2 Result and discussion

4.2.1 Absorption line search

As mentioned in 4.1, We chose a wavelength range around 1.5μm. There are some options of absorption lines for isotopic measurement according previous research, however, we found several inconsistencies between the result of the previous research and the spectra measured with our CRDS. So, we searched the absorption lines using $^{15}NH_3$ standard gas (Table3) with a purity of 98%.

The results are shown in Figure 22. The measurement pressure was 2 Pa, and the spectral range corresponded to 1494.5 $\sim$ 1495.5 nm. Seventeen peaks exceeding SNR $\sim$ 100 were observed. Finally, three peaks were picked up from these candidates for isotopic measurement. We selected carefully according to the following two points: (i) there is a $^{15}NH_3$ absorption line close in intensity to the

$^{15}NH_3$ absorption line, specifically, the difference in those intensities is smaller than the dynamic range of this CRDS, and (ii) those peaks and the surrounding peaks are separatable enough to recognize the peak centers.

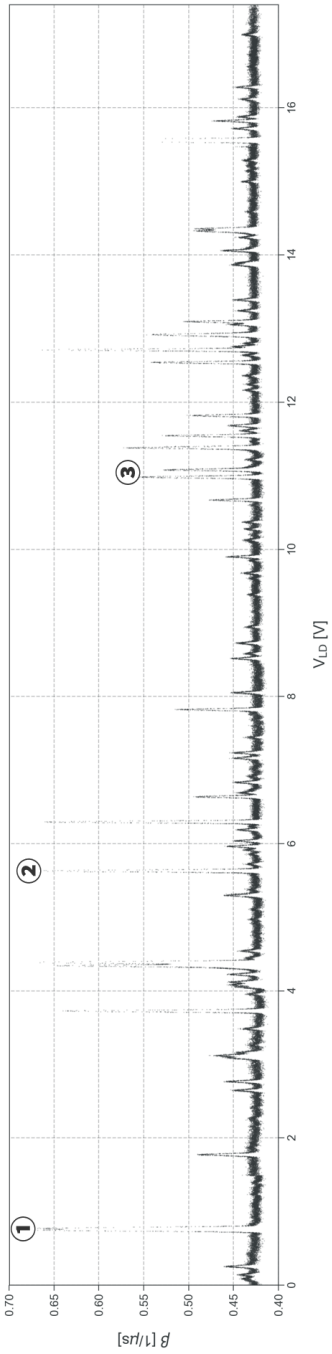

Figure 22 Absorption spectral of $^{15}NH_3$ standard gas at 2 Pa. The Horizontal axis correspond to the laser wavelength that the range is 1494.5 $\sim$ 1495.5nm. ① $\sim$ ③ correspond to Region-1 $\sim$ Region-3 in 4.2.2, respectively, picked up to measure in detail for isotopic analysis.

4.2.2 Precision study

One of the purposes of this study is to verify the precision of this CRDS in isotopic measurement. We performed, based on the point, measurement of the above three $^{15}NH_3$ absorption lines in detail. NH_3 gas (Table3) was measured continuously for six hours, and the variations were observed. To evaluate the variance of the time series data, we defined a value based on Allan variance:

$$\sigma\langle\delta^{15}N\rangle^2_{\mathrm{avar}}(t_w) = \frac{1}{2\,(n-1)}\sum_{i}^{n-1}\left(\langle\delta^{15}N\rangle_{i+1}\,(t_w) - \langle\delta^{15}N\rangle_{i}\,(t_w)\right)^2 \qquad (28)$$

where n is the number of data and t_w is the time window to divide the time series of ring-down data for calculating δ^{15}N. When the whole measurement time is 300 minutes and $t_w = 5$ minutes, for example, the δ values are got as $\langle\delta^{15}\mathrm{N}\rangle_i\,(t_w = 5\mathrm{min})$: $\langle\delta^{15}\mathrm{N}\rangle_1, \langle\delta^{15}\mathrm{N}\rangle_2, \ldots \langle\delta^{15}\mathrm{N}\rangle_{60}$. Allan variance represents the variance of the time series data within a time window, so can be used for optimizing measurement time. In this measurement, the mean value of R was used as R_0 (cf., equation 25).

First, Region-1 includes the absorption line near 1494.2 nm (Figure 23). This peak was slightly interfered with by a large saturated peak. B. Lins et al. (2010) described this single peak, but actually it was double peaks that were close to each other. This was supposedly coursed by the tunneling effect through the potential barrier formed by the structure of ammonia molecule. When the three hydrogens are labeled uniquely, the conformations with the nitrogen pointing up and down are not superimposable. These two conformations form potential wells on each side, consequently the absorption peak splits. Thus, to simplify the calculation, we calculated ^{15}N / ^{14}N by $(A_{\mathrm{P1a}} + A_{\mathrm{P1b}})/2A_{\mathrm{P2}}$ with assumption that S_{P1a} and S_{P1b} is equal.

Second, Region-2 includes the absorption line near 1494.9 nm (Figure 24). A large peak is dominant also in this region. There is a single $^{15}NH_3$ peak, however these peaks interfere more seriously. Over-fitting in the area of the saturated peak will have a direct influence on the estimation of the P1 shape. ^{15}N / ^{14}N was calculated by $A_{\mathrm{P1}}/A_{\mathrm{P2}}$.

Third, Region-3 includes the absorption line near 1495.8 nm (Figure 25). This region includes only two peaks, and they also interfere with each other. The $^{15}NH_3$ peak is relatively smaller than the $^{14}NH_3$ peak, however, the fitting calculation is simpler than other cases.

$\delta^{15}N$ time series of each wavelength region in the case of t_w = 1.7, 8.3, 15.0 minutes are shown in Figure 26 $\sim$ 28. In Region-1 and Region-2, over-fitting occurred at smaller t_w. Its cause was over-fitting in the saturated area because of a lack of ring-down data points. Whether there is a saturated peak or not influence significantly on the spectrum analysis. In addition, the fluctuations were sometimes observed near the start (e.g., Figure 26). This trend had a period of several ten minutes, considered to be caused by diffusion of the injected sample.

Figure 29 $\sim$ 31 shows the Allan variance at different t_w in each Region. σ_{avar} decreased with t_w increasing, and converged at t_w around 10 minutes in all Regions. This corresponds to about 1500 ring-downs for Region-3 with the setup in this study. The wavelength region with the best precision resulted in Region-3, where the σ_{avar} was approximately 15‰.

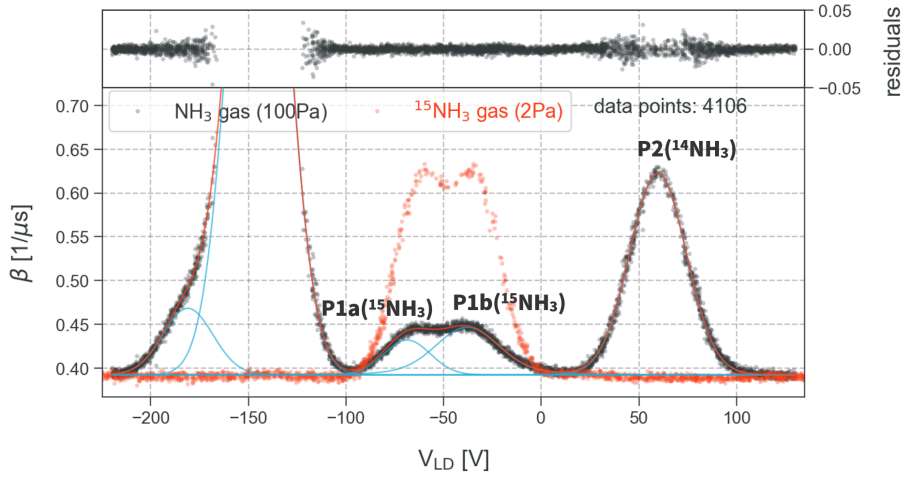

Figure 23 Absorption spectra at t_w = 10 minutes in Region-1. The Horizontal axis is the input voltage to the LD controller, corresponding to the laser wavelength where is 1494.2 nm at $V_{\mathrm{LD}} = 0$. The wavelength range is approximately 0.03nm. Black and Red points represent the β values of NH_3 gas and $^{15}NH_3$ standard gas samples. Blue lines represent each single peak fitted with Voigt model, and a red line represents the summation of these peaks.

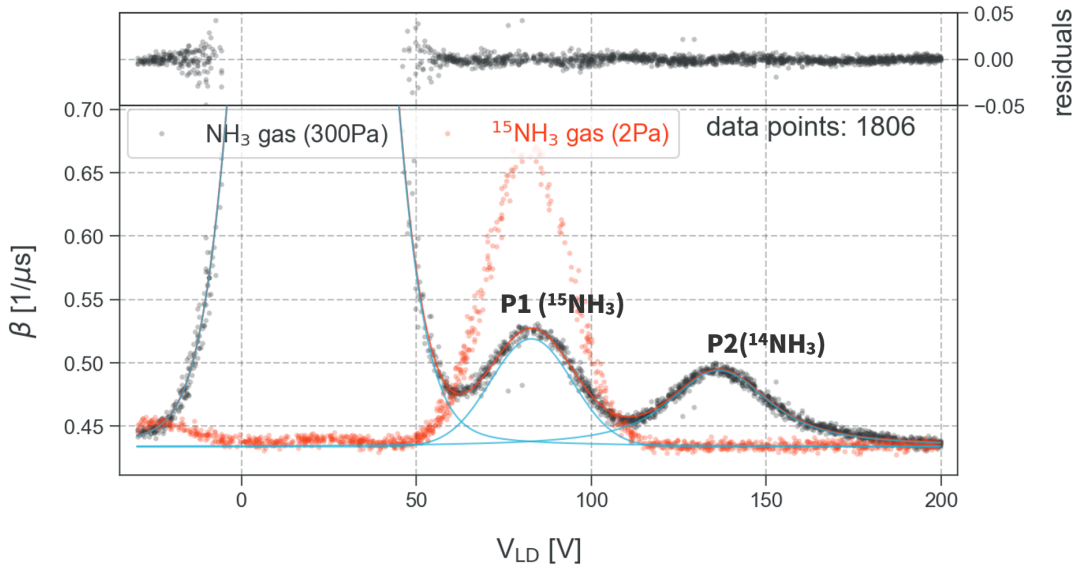

Figure 24 Absorption spectra at $t_w = 10$ minutes in Region-2. The laser wavelength is 1494.9 nm at $V_{\mathrm{LD}} = 0$. The wavelength range is approximately 0.0nm.

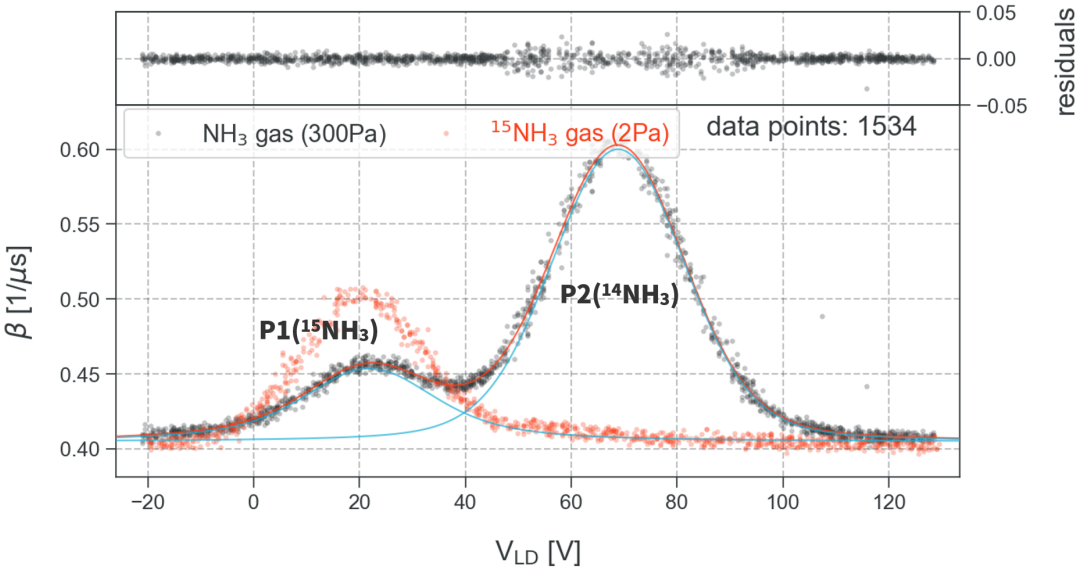

Figure 25 Absorption spectra at $t_w = 10$ minutes in Region-3. The laser wavelength is 1495.8 nm at $V_{\mathrm{LD}} = 0$. The wavelength range is approximately 0.015nm.

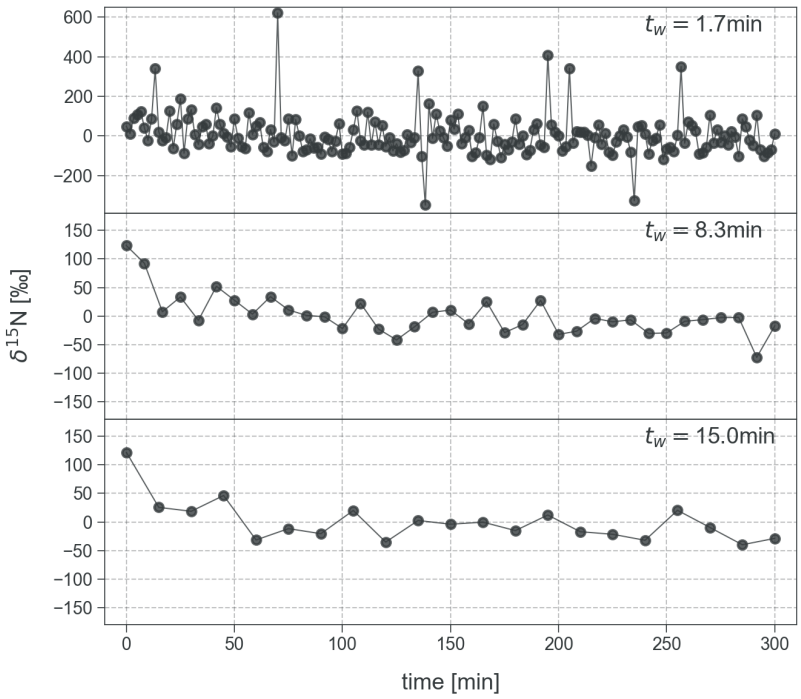

Figure 26 Time series of $\delta^{15}N$ calculated from Region-1 spectra.

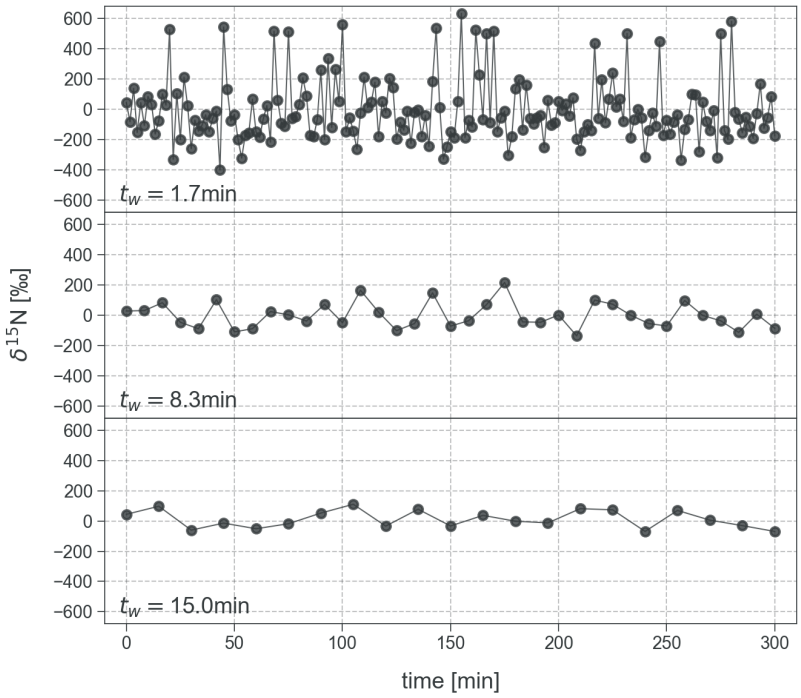

Figure 27 Time series of $\delta^{15}N$ calculated from Region-2 spectra.

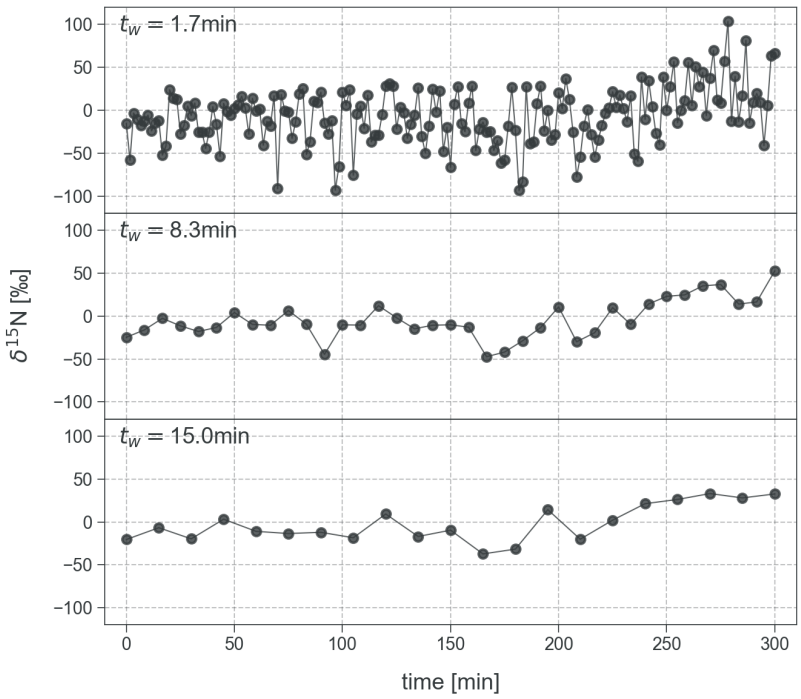

Figure 28 Time series of $\delta^{15}N$ calculated from Region-3 spectra.

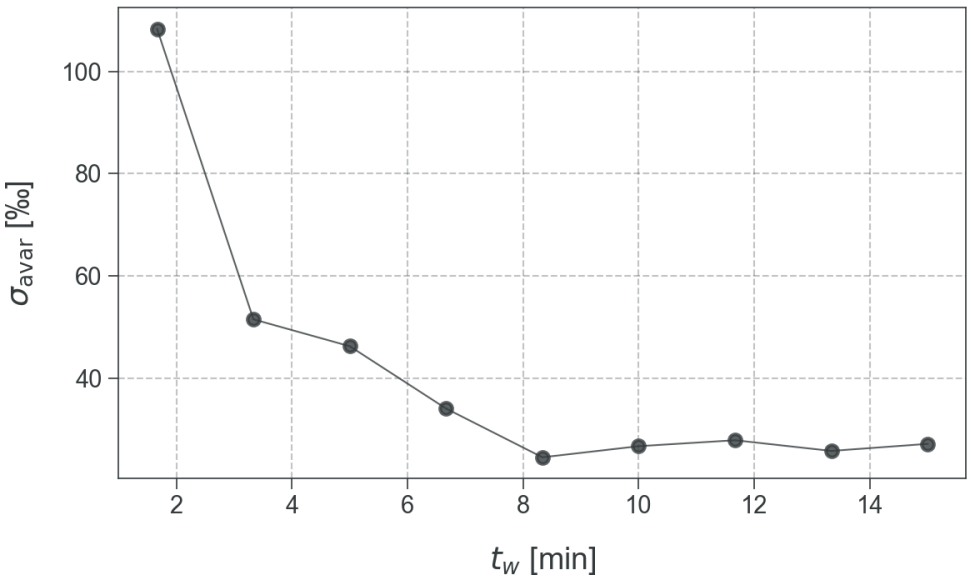

Figure 29 Allan variance of Region-1.

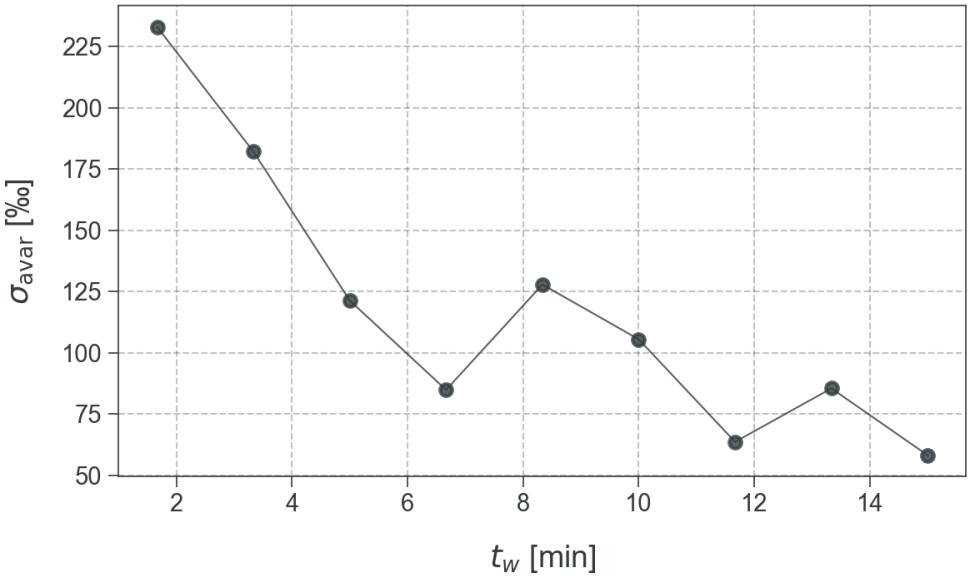

Figure 30 Allan variance of Region-2.

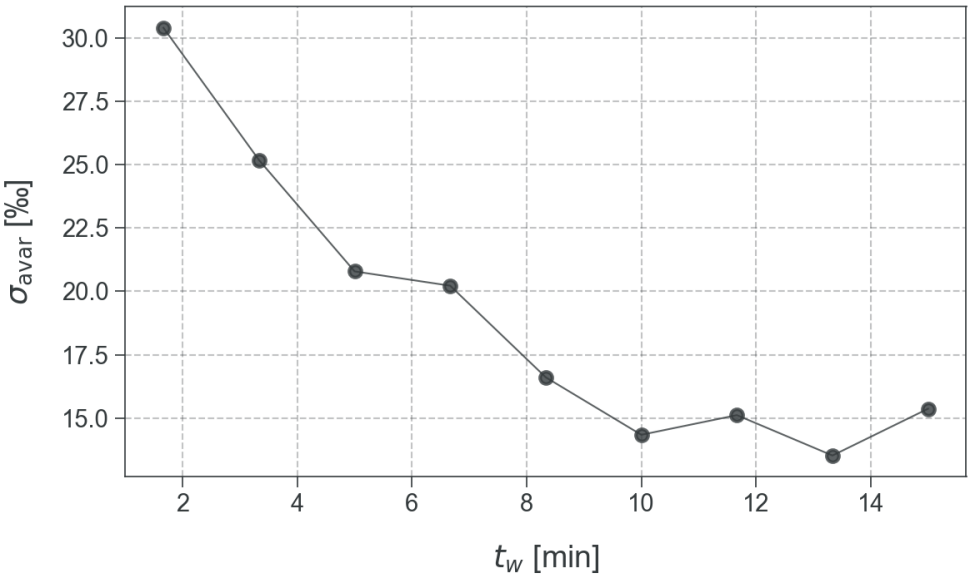

Figure 31 Allan variance of Region-3.

4.2.3 Accuracy study

Another purpose of this study is to prove the ability in isotopic ratio, in other words the accuracy. We prepared mixtures of NH_3 gas and $^{15}NH_3$ standard gas as isotopic samples before introducing them to the CRDS cavity, and measured with different amounts of $^{15}NH_3$ standard gas input. We defined this input amount as I_{sample}. A schematic of the sample line is presented in Figure 20. First, N_2 and NH_3 gas was introduced to the tank with a ratio of 100 : 1. This is because the typical abundance of ammonia in a planetary environment is 1 % according to the previous observation [34]. Then the valve was opened and the sample gas was introduced to the cavity. After that, pressure in the cavity was adjusted to a measurable range, specifically 200 Pa in this measurement. After that, $^{15}NH_3$ standard gas was introduced with a controlled amount using gas Syringe. Thus, we obtained a calibration plot between measured $\delta^{15}N$ and I_{sample}, assuming the R_0 (cf. Equation 25) to be R at $I_{\mathrm{sample}} = 0$ μL. Taking the precision study into consideration, we measured with the time window of 10 minutes, then took an average of five times of measurement in each I_{sample}.

On the other hand, we measured an absorption spectrum of only the $^{15}NH_3$ standard gas at 7.7 Pa with the input amount of 100 μL (Figure 32). Now the $^{15}NH_3$ amount in NH_3 gas at $I_{\mathrm{sample}} = 0$ μL is known:

$$p_{\mathrm{ini}} = 7.7 \times \frac{A_{\mathrm{ini}}}{A_{\mathrm{st}}} \tag{29}$$

where A_{ini} and A_{st} are the P1 area (cf. Figure 33) when $I_{\mathrm{sample}} = 0$ μL and of the $^{15}NH_3$ standard gas, respectively. Then finally the axis of the $^{15}NH_3$ standard gas input in the calibration plot can be converted to true $\delta^{15}N$ (Figure 34):

$$\delta^{15}N_{\mathrm{true}} = \left[\frac{(p_{\mathrm{ini}} + p_{\mathrm{add}}) \,/\, (200 - p_{\mathrm{ini}})}{R_{\mathrm{ini}}} - 1 \right] \times 1000 \tag{30}$$

$$p_{\mathrm{add}} = 0.077 \times I_{\mathrm{sample}} \tag{31}$$

$$R_{\mathrm{ini}} = \frac{p_{\mathrm{ini}}}{200 + p_{\mathrm{ini}}} \tag{32}$$

The calibration line showed good agreement between measured and true values, with a the slope of 1.01 and an R-squared of 0.9989.

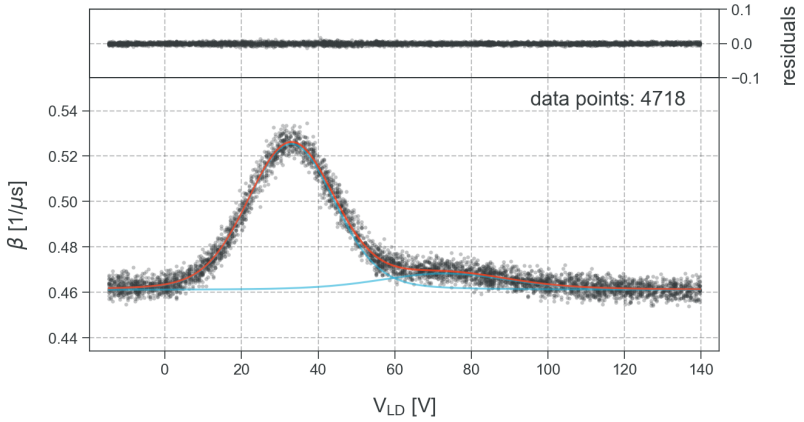

Figure 32 Spectrum of $^{15}NH_3$ standard gas at 7.7 Pa. The wavelength range is the same as Figure 33.

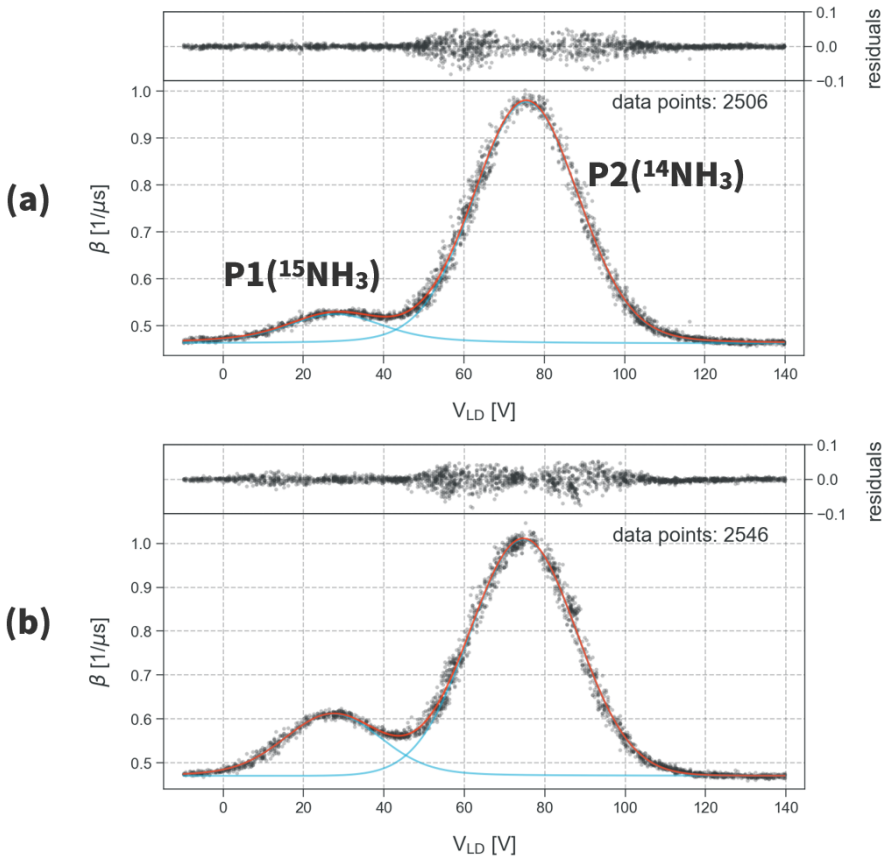

Figure 33 Spectra of mixtures of NH_3 and $^{15}NH_3$ standard gas at (a) I_{iso} = 0 μL and (b) I_{iso} = 100 μL.

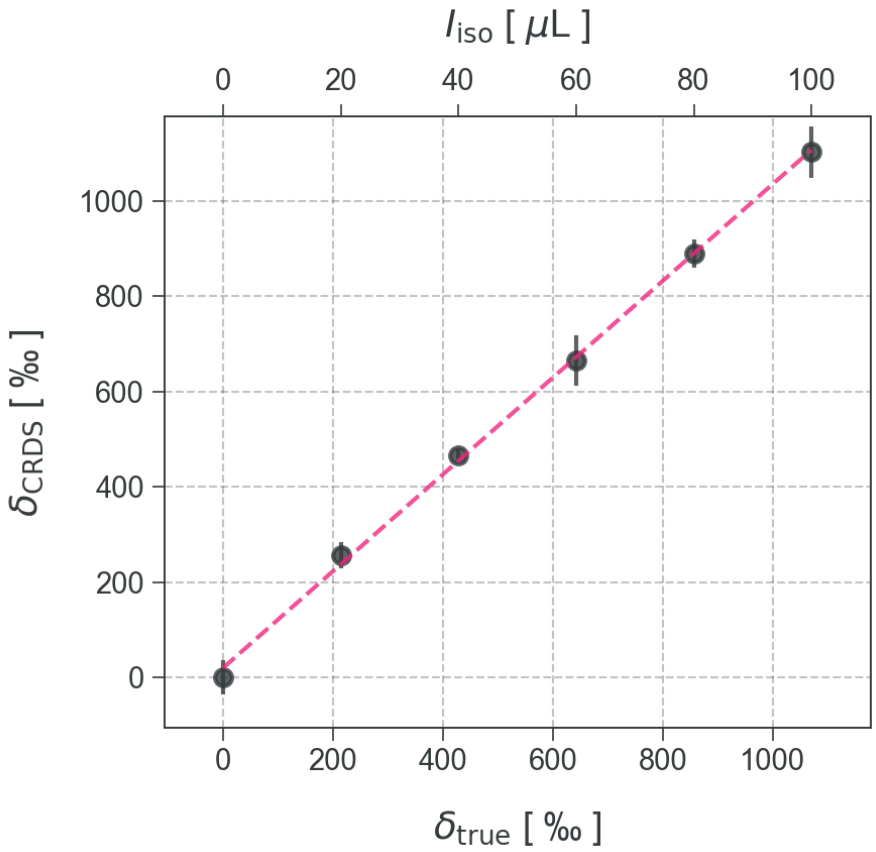

Figure 34 Calibration plot of $^{15}NH_3$ isotopes sample. The Horizontal axis, $\delta^{15}N_{\mathrm{true}}$ is the isotopic ratio calculated from introduced amount of $^{15}NH_3$ standard gas I_{sample}. The vertical axis is the measured isotopic ratio assuming the value at $I_{\mathrm{iso}} = 0$ as R_0.

4.3 Conclusion

This study is the a new achievement as the isotopic measurement of NH_3 with CRDS. We started from the exploration of ammonia absorption lines, and found several candidates derived from $^{15}NH_3$ in the region around 1595 nm. In the precision study, we confirmed that the measurement using one of the candidates, which located at 1495.8 nm, achieved variance ±7.5 ‰ in δ^{15}N. In the accuracy study, we measured samples with different isotopic ratios, and obtained the calibration line. It was in good agreement between measured and true values, where the R-squared was 0.9989 and the residual at 100 ‰ fractionation was 1 ‰. Considering the range of δ^{15}N in the solar system components is -400 ∼ 1000 ‰, our CRDS

with 50cm cavity using 1.5 μm laser exhibited enough precision and accuracy for ammonia isotopic ratio.

In the future study, it is expected the down-sizing of the whole system. Further, measurement of deuterated ammonia should also be attempted. NH_2D/NH_3 observation in icy bodies might give a constraint on the origin of the Deuterium Enrichment in the Solar System. Because of its light-weight and high-sensitivity, we consider the CRDS to be an effective method of isotopic investigation in the outer region of the solar system, where cost a lot to reach.

5 General conclusion and prospection

As the result of this study, we concluded our CRDS, even though it consists of a small and simple measuring system with a 5cm cavity, has a enough ability to measure an isotopic ratio with precision in the order of 10 ‰. We obtained calibration lines of δD in water and δ^{15}N in ammonia, and these were in good agreement between literature and measured values with a precision of up to 1 ‰. The CRDS showed high-sensitivity in a measurement of D-depleted water isotopic ratio. The SNR of the HDO absorption peak used in this study was 7.17 with -987 $\pm$ 19 ‰in δD. Furthermore, the δ^{15}N measurement of ammonia is a new attempt in the use of CRDS. We didn't achieve precise measurements for oxygen isotopes in water vapor that require an accuracy under 10 ‰. However, as we can be seen from the good agreement of ammonia isotopic calibration with the cavity of ten times length, in which the accuracy was up to 1 ‰, theoretically it must be cleared in the future study.

Another achievement of our CRDS is the batch measurement system, but not flow. Because the sample is entirely sealed between the measurement, it can reduce a sample waste. This method will be a great advantage on the usage in an environment with a trace sample amount, like the moon surface. In addition, a relative measurement become available by carrying a few amount of the isotopic standard sample, which is robust against the contamination biases.

In the future, it is expected to explore the outer region of the solar system, especially icy bodies. The volatile molecules in this region potentially preserve the end-members of the isotopic compositions, because they exist mainly in the solid state. However, most of the isotopes are not observed directory yet. CRDS, which

is compact and high-sensitivity spectroscopy method, can measure the isotopic ratio of these volatile molecules without destruction, for example H_2O, CO_2, NH_3, CH_4, HCN, etc. In this study, we proved the potential of the CRDS in H_2O and NH_3 isotopic measurement. In addition, CO_2 was already measured in The Mars Curiosity mission. There are many absorption bands in infrared region which include enough high-intensity transitions, and light sources are well-developed in this region (Figure 35). We will be able to measure the isotopes of all the species with high wavelength resolution and high-sensitivity, by carefully choosing laser wavelength. If we use multiple wavelength bands, optical switching system is available (MEMS, AOM, etc.).

Thus, we proposed CRDS is a useful method for in-situ isotopic measurement of volatile molecules, particularly H_2O and NH_3. First in the future, let's look at the reveal of Hydrogen isotopic ratio in the Moon water by CRDS.

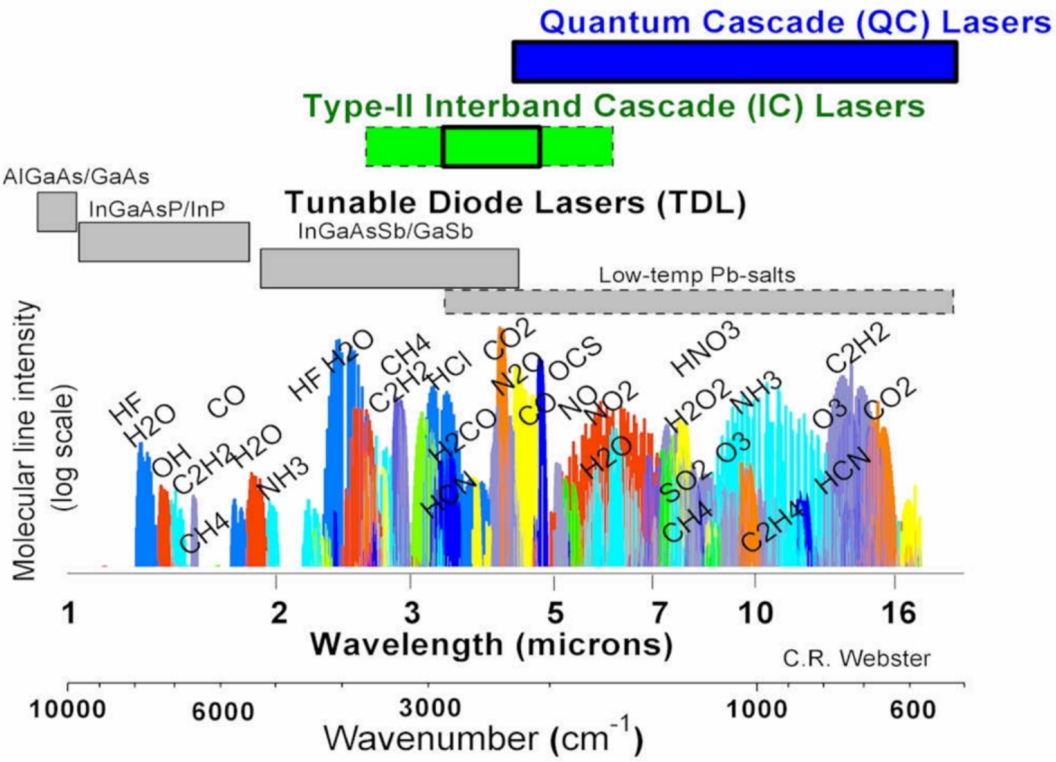

Figure 35 Absorption line intensities in infrared region and available laser light sources. (Cited from [40])

Acknowledgements

I would like to show my extremely appreciation to my supervisors, Prof. Chihiro Yamanaka of Osaka University for his continuous support throughout every stage of the research project. His tutelage with great depth of knowledge and invaluable generosity encouraged me in all time of my study life. I would like to express my gratitude to Prof. Kentaro Terada insightful comments and suggestions from the perspective of planet science and as the leader of a laboratory. In addition, I would like to thank Prof. Ko Hashizume in Ibaraki University for his powerful encouragement. I would also like to thank all the members of Terada laboratory for the valuable discussions and the fun times.

This study was partially supported by the Space Exploration Innovation Hub Research (2016 - 2019) at JAXA, and the collaboration research fund at Institute of Laser Engineering, Osaka University.

Finally, I specially thank my family. it would be impossible for me to complete my study without their tremendous support and understandings.

List of publications and presentations

Peer-reviewed paper

Junpei Murayama, Chihiro Yamanaka, Ko Hashizume, Shun Takigami, "D-depleted water isotopic measurement with a miniaturized cavity ring-down spectrometer aiming for exploration of lunar water", Sens. Actuators A-Phys., 338, 113481, 2022.

Presentations in international conference

1. Chihiro Yamanaka Ko Hashizume, Junpei Murayama, Naoya Tasaka, "Development of CRDS (Cavity Ring-down Spectroscopy) aiming water isotope measurements on the moon", Japan Geoscience Union Meeting 2018, Chiba, Japan, May 2018.

2. Junpei Murayama, Chihiro Yamanaka、Ko Hashizume, Hisashi Abe and Shun Takigami, "Miniaturized Cavity Ring-Down Spectrometer with 5 cm Cavity for Water Isotopic Measurements", 8th International Conference on Sensors Engineering and Electronics Instrumentation Advances, Corfu, Greece, September 2022.

References

[1] S. Nozette, C. L. Lichtenberg, P. Spudis, R. Bonner, W. Ort, E. Malaret, M. Robinson, E. M. Shoemaker, "The Clementine Bistatic Radar Experiment", Science, 274, 1495-1498, 1996.

[2] W. C. Feldman, S. Maurice, A. B. Binder, B. L. Barraclough, R. C. Elphic, D. J. Lawrence, "Fluxes of Fast and Epithermal Neutrons from Lunar Prospector: Evidence for Water Ice at the Lunar Poles", Science, 281, 1496-1500, 1998.

[3] R. N. Clark, "Detection of Adsorbed Water and Hydroxyl on the Moon", Science, 326, 562-564, 2009.

[4] J. M. Sunshine, T. L. Farnham, L. M. Feaga, O. Groussin, F. Merlin, R. E. Milliken, M. F. A'Hearn, "Temporal and Spatial Variability of Lunar Hydration As Observed by the Deep Impact Spacecraft", Science, 326, 565-568, 2009.

[5] C. M. Pieters, J. N. Goswami, R. N. Clark, M. Annadurai, J. Boardman, B. Buratti, J-P. Combe, M. D. Dyar, R. Green, J. W. Head, C. Hibbitts, M. Hicks, P. Isaacson, R. Klima, G. Kramer, S. Kumar, E. Livo, S. Lundeen, E. Malaret, T. McCord, J. Mustard, J. Nettles, N. Petro, C. Runyon, M. Staid, J. Sunshine, L. A. Taylor, S. Tompkins, P. Varanasi, "Character and Spatial Distribution of OH/H_2O on the Surface of the Moon Seen by M^3 on Chandrayaan-1", Science, 326, 568-572, 2009.

[6] A. Colaprete, P. Schultz, J. Heldmann, D. Wooden, M. Shirley, K. Ennico, B. Hermalyn, W. Marshall1, A. Ricco, R. C. Elphic, D. Goldstein, D. Summy, G. D. Bart, E. Asphaug, D. Korycansky, D. Landis, L. Sollitt, "Detection of Water in the LCROSS Ejecta Plume", Science, 330, 463-468, 2010.

[7] P. G. Lucey, G. A. Neumann, M. A. Riner, E. Mazarico, D. E. Smith, M. T. Zuber, D. A. Paige, D. B. Bussey, J. T. Cahill, A. McGovern, P. Isaacson, L. M. Corley, M. H. Torrence, H. J. Melosh, J. W. Head, E. Song, "The global albedo of the Moon at 1064 nm from LOLA", JGR: Planets, 119, 1665-1679, 2014.

[8] O. J. Tucker, W. M. Farrell, R. M. Killen and D. M. Hurley, "Solar Wind Implantation Into the Lunar Regolith: Monte Carlo Simulations of H Retention in a Surface With Defects and the H_2 Exosphere", J. Geophys. Res. Planets,

124, 278-293, 2019.

[9] M. Benna, D. M. Hurley, T. J. Stubbs, P. R. Mahaffy, R. C. Elphic, “Lunar soil hydration constrained by exospheric water liberated by meteoroid impacts”, Nat. Geosci., 12, 333-338, 2019.

[10] Yi Chen, Sen Hu, Jin-Hua Li, Qiu-Li Li, Xiongyao Li, Yang Li, Yang Liu, Yuqi Qian, Wei Yang, Qin Zhou, Yangting Lin, Chunlai Li, Xian-Hua Li, “Chang’e-5 lunar samples shed new light on the Moon”, The Innovation Geoscience, 1, 1, 2023.

[11] Honglei Lin, Shuai Li, Rui Xu, Yang Liu, Xing Wu, Wei Yang, Yong Wei, Yangting Lin, Zhiping He, Hejiu Hui, Huaiyu He, Sen Hu, Chi Zhang, Chunlai Li, Gang Lv, Liyin Yuan, Yongliao Zou, Chi Wang, “In situ detection of water on the Moon by the Chang’E-5 lander”, Sci. Adv., 8, 1, 2022.

[12] Jianjun Liu, Bin Liu, Xin Ren, Chunlai Li, Rong Shu, Lin Guo, Songzheng Yu, Qin Zhou, Dawei Liu, Xingguo Zeng, Xingye Gao, Guangliang Zhang, Wei Yan, Hongbo Zhang, Lihui Jia, Shifeng Jin, Chunhua Xu, Xiangjin Deng, Jianfeng Xie, Jianfeng Yang, Changning Huang, Wei Zuo, Yan Su, Weibin Wen, Ziyuan Ouyang, “Evidence of water on the lunar surface from Chang’E-5 in-situ spectra and returned samples”, Nat. Commun. , 13, 3119, 2022.

[13] P. R. Mahaffy, C. R. Webster, S. K. Atreya, H. Franz, M. Wong, P. G. Conrad, D. Harpold, J. J. Jones, L. A Leshin, H. Manning, T. Owen, R. O. Pepin, S. Squyres, M. Trainer, “Abundance and Isotopic Composition of Gases in the Martian Atmosphere from the Curiosity Rover”, Science, 341, 263-266, 2013.

[14] C.R. Webster et al., “Isotope Ratios of H, C, and O in CO2 and H2O of the Martian Atmosphere”, Science, 341, 260-263, 2013.

[15] M. Wieser, S. Barabash, Y. Futaana, M. Holmström, A. Bhardwaj, R. Sridharan, M. B. Dhanya, P. Wurz, A. Schaufelberger, K. Asamura, ”Extremely high reflection of solar wind protons as neutral hydrogen atoms from regolith in space”, Planet Space Sci, 57, 2132-2134, 2009.

[16] A. Bhardwaj, M B Dhanya, A. Alok, S. Barabash, M. Wieser, Y. Futaana, P. Wurz, A. Vorburger, M. Holmström, C. Lue, Y. Harada, K. Asamura, ”A new view on the solar wind interaction with the Moon”, Geoscience Letters, 2, 10, 2015.

[17] P. Borin, G. Cremonese, F. Marzari and A. Lucchetti, ”Asteroidal and cometary dust flux in the inner solar system”, astronomy and astrophysics, 605, 12, 2017.

[18] K. Altwegg, H. Balsiger, A. Bar-Nun, J. J. Berthelier, A. Bieler, P. Bochsler, C. Briois, U. Calmonte, M. Combi, J. De Keyser, P. Eberhardt, B. Fiethe, S. Fuselier, S. Gasc, T. I. Gombosi, K.C. Hansen, M. Hässig, A. Jäckel, E. Kopp, A. Korth, L. LeRoy, U. Mall, B. Marty, O. Mousis, E. Neefs, T. Owen, H. Rème, M. Rubin, T. Sémon, C.-Y. Tzou, H. Waite, P. Wurz, "67P/Churyumov-Gerasimenko, a Jupiter family comet with a high D/H ratio", Science, 347, 1261952, 2015.

[19] D. J. Rhodes, W. M. Farrell, "Mapping the Predicted Solar Wind Hydrogen Flux in Lunar South Pole Craters", Planet. Sci. j. 1, 13, 2020.

[20] L. J. Hallis, "D/H ratios of the inner Solar System", Philos. Trans. Royal. Soci. A, 375, 1471-2962, 2017.

[21] K. D. McKeegan, A. P. A. Kallio, V. S. Heber, G. Jarzebinski, P. H. Mao, C. D. Coath, T. Kunihiro, R. C. Wiens, J. E. Nordholt, R. W. Moses Jr, D. B. Reisenfeld, A. J. G. Jurewicz, D. S. Burnett, "The oxygen isotopic composition of the Sun inferred from captured solar wind", Science, 332, 6037, 1528-1532, 2011.

[22] K. Hashizume, M. Chaussidon , "A non-terrestrial ^{16}O-rich isotopic composition for the protosolar nebula", Nature, 434, 619-622, 2005.

[23] K. Hashizume, N. Takahata, H. Naraoka, Y. Sano, "Extreme oxygen isotope anomaly with a solar origin detected in meteoritic organics", Nat. Geosci., 4, 165-168, 2011.

[24] N. Sakamoto, Y. Seto, S. Itoh, K. Kuramoto, K.i Fujino, K. Nagashima, A. N Krot, H. Yurimoto, "Remnants of the early solar system water enriched in heavy oxygen isotopes". Science, 317, 231-233, 2007.

[25] K. Terada, S. Yokota, Y. Saito, N. Kitamura, K. Asamura, M. N. Nishino, "Biogenic oxygen from Earth transported to the Moon by a wind of magnetospheric ions", Nat Astron, 1, 0026, 2017.

[26] H. Abe, K. Hashiguchi, D. Lisak, S. Honda, T. Miyake, H. Shimizu, "A miniaturized trace-moisture sensor based on cavity ring-down spectroscopy", Sens. Actuators A-Phys., 320, 112559, 2021.

[27] Lyndon B. Johnson Space Center, "Apollo 17 Preliminary Science Report", NASA, 1973.

[28] J. H. Hoffman, R. R. Hodges Jr., "Molecular gas species in the lunar atmosphere", The Moon, 14, 159-167, 1975.

[29] C. T. Russell, C. A. Raymond, "The Dawn mission to Vesta and Ceres",

Space Sci. Rev. 163, 3-23, 2011.

[30] M. C. De Sanctis, E. Ammannito, A. Raponi, S. Marchi, T. B. McCord, H. Y. McSween, F. Capaccioni, M. T. Capria, F. G. Carrozzo, M. Ciarniello, A. Longobardo, F. Tosi, S. Fonte, M. Formisano, A. Frigeri, M. Giardino, G. Magni, E. Palomba, D. Turrini, F. Zambon, J.-P. Combe, W. Feldman, R. Jaumann, L. A. McFadden, C. M. Pieters, T. Prettyman, M. Toplis, C. A. Raymond, C. T. Russell, "Ammoniated phyllosilicates with a likely outer Solar System origin on (1) Ceres", Nature, 528, 241-244, 2015.

[31] T. V. V. King, R. N. Clark, W. M. Calvin, D. M. Sherman, R. H. Brown, "Evidence for ammonium-bearing minerals on Ceres", Science, 255, 1551-1553, 1992.

[32] S. K. Singh, A. Bergantini, C. Zhu, M.o Ferrari, M. Cristina De Sanctis, S. De Angelis, R. I. Kaiser, "Origin of ammoniated phyllosilicates on dwarf planet Ceres and asteroids", Nat Commun, 12, 2690, 2021.

[33] M. Choukroun, O. Grasset, "Thermodynamic data and modeling of the water and ammonia-water phase diagrams up to 2.2 GPa for planetary geophysics", J. Chem. Phys., 133, 144502, 2010.

[34] J. H. Waite Jr, W. S. Lewis, B. A. Magee, J. I. Lunine, W. B. McKinnon, C. R. Glein, O. Mousis, D. T. Young, T. Brockwell, J. Westlake, M.-J. Nguyen, B. D. Teolis, H. B. Niemann, R. L. McNutt Jr, M. Perry, W.-H. Ip, 'Liquid water on Enceladus from observations of ammonia and 40Ar in the plume", Nature, 460, 487-490, 2009.

[35] E. Furi, B. Marty, "Nitrogen isotope variations in the Solar System", Nat. Geosci., 8, 515-522, 2015.

[36] T. Owen, P. R. Mahaffy, H. B. Niemann, S. Atreya, M. Wong, "Protosolar nitrogen", Astrophys. J., 553, L77-L79, 2001.

[37] Y. Shinnaka, H. Kawakita, H. Kobayashi, M. Nagashima, D. C. Boice, "$^{14}NH_2/15NH_2$ ratio in Comet C/2012 S1 (ISON) observed during Its Outburst in 2013 November", Astrophys. J. Lett., 553, L77-L79, 2001.

[38] H. B. Niemann, S. K. Atreya, J. E. Demick, D. Gautier, J. A. Haberman, D. N. Harpold, W. T. Kasprzak, J. I. Lunine, T. C. Owen, F. Raulin, "Composition of Titan's lower atmosphere and simple surface volatiles as measured by the Cassini-Huygens probe gas chromatograph mass spectrometer experiment". J. Geophys. Res. 115, E12006, 2010.

[39] B. Lins, F. Pflaum, R. Engelbrecht, B. Schmauss, "Absorption line strengths

of 15NH3 in the near infrared spectral region", Appl. Phys. B, 102, 293-301, 2011.

[40] C. R. Webster, J. R. Mahaffy, "Measuring Methane & its Isotopic Ratios $^{13}C/^{12}C$ and D/H with the Tunable Laser Spectrometer (TLS) on SAM for the Mars Science Laboratory (MSL) Mission", Joint ESA-ASI Workshop on Methane on Mars ESA/ ESRIN, Frascati, Italy, November 2009.

[41] I. E. Gordon, L. S. Rothman, C. Hill, R. V. Kochanov, Y.Tan, P .F. Bernath, M. Birk, V. Boudon, A. Campargue, K. V. Chance, B. J. Drouin, J. -M. Flaud, R. R. Gamache, J.T. Hodges, D. Jacquemart, V. I. Perevalov, A. Perrin, K.P. Shine, M. -A. H. Smith, J. Tennyson, G. C. Toon, H. Tran, V. G. Tyuterev, A. Barbe, A. G. Császár, V. M. Devi, T. Furtenbacher, J. J. Harrison, J. -M. Hartmann, A. Jolly, T. J. Johnson, T. Karman, I. Kleiner, A. A. Kyuberis, J. Loos, O. M. Lyulin, S. T. Massie, S. N. Mikhailenko, N. Moazzen-Ahmadi, H. S. P. Müller, O. V. Naumenko, A. V. Nikitin, O. L. Polyansky, M. Rey, M. Rotger, S. W. Sharpe, K. Sung, E. Starikova, S. A. Tashkun, J. Vander Auwera, G. Wagner, J. Wilzewski, P. Wcisto, S. Yu, E. J. Zak, "The HITRAN2016 molecular spectroscopic database", J. Quant. Spectrosc. Ra. Transf. 203, 3-69, 2017.

[42] R. V. Kochanov, I. E. Gordon, L. S. Rothman, P. Wcisto, C. Hill, J. S. Wilzewski, "HITRAN Application Programming Interface (HAPI): A comprehensive approach to working with spectroscopic data", J. Quant. Spectrosc. Ra. Transf. 177, 15-30, 2016.